Monthly Notices
of the
ROYAL ASTRONOMICAL SOCIETY

Mon. Not. R. Astron. Soc. **419,** 2264–2292 (2012) doi:10.1111/j.1365-2966.2011.19881.x

The near-IR $M_{\rm bh}$–L and $M_{\rm bh}$–n relations

Marina Vika,[1⋆] Simon P. Driver,[1] Ewan Cameron,[2] Lee Kelvin[1] and Aaron Robotham[1]

[1]*Scottish Universities Physics Alliance (SUPA), School of Physics & Astronomy, University of St Andrews, North Haugh, St Andrews, Fife KY16 9SS*
[2]*Department of Physics, Swiss Federal Institute of Technology (ETH-Zürich), CH-8093 Zürich, Switzerland*

Accepted 2011 September 22. Received 2011 September 22; in original form 2010 December 10

ABSTRACT

We present near-infrared (near-IR) surface photometry (2D profiling) for a sample of 29 nearby galaxies for which supermassive black hole (SMBH) masses are constrained. The data are derived from the UKIDSS-LAS representing a significant improvement in image quality and depth over previous studies based on Two Micron All Sky Survey data. We derive the spheroid luminosity and spheroid Sérsic index for each galaxy with GALFIT3 and use these data to construct SMBH mass–bulge luminosity ($M_{\rm bh}$–L) and SMBH–Sérsic index ($M_{\rm bh}$–n) relations. The best-fitting K-band relation for elliptical and disc galaxies is $\log(M_{\rm bh}/{\rm M}_{\odot}) = -0.36(\pm0.03)(M_K + 18) + 6.17(\pm0.16)$, with an intrinsic scatter of $0.4^{+0.09}_{-0.06}$ dex, whilst for elliptical galaxies we find $\log(M_{\rm bh}/{\rm M}_{\odot}) = -0.42(\pm0.06)(M_K + 22) + 7.5(\pm0.15)$, with an intrinsic scatter of $0.31^{+0.087}_{-0.047}$ dex. Our revised $M_{\rm bh}$–L relation agrees closely with the previous near-IR constraint by Graham. The lack of improvement in the intrinsic scatter in moving to higher quality near-IR data suggests that the SMBH relations are not currently limited by the quality of the imaging data but is either intrinsic or a result of uncertainty in the precise number of required components required in the profiling process. Contrary to expectation, a relation between SMBH mass and the Sérsic index was not found at near-IR wavelengths. This latter outcome is believed to be explained by the generic inconsistencies between 1D and 2D galaxy profiling which are currently under further investigation.

Key words: galaxies: bulges – galaxies: elliptical and lenticular, cD – galaxies: fundamental parameters – galaxies: nuclei – galaxies: photometry – galaxies: structure.

1 INTRODUCTION

The number of supermassive black hole (SMBH) mass measurements ($M_{\rm bh}$) from inactive galaxies in the local Universe have rapidly increased over the last 15 yr (see Graham et al. 2011, hereafter GO11, for sample compilation). Kormendy & Richstone (1995) reviewed $M_{\rm bh}$ determinations for a sample of eight local galaxies and introduced the SMBH mass ($M_{\rm bh}$)–galaxy luminosity (L, or bulge luminosity in the case of disc galaxies) relation.[1] Since this time, the $M_{\rm bh}$–L correlation has been investigated by a number of groups from optical to near-infrared (near-IR) passbands (Magorrian et al. 1998; Kormendy & Gebhardt 2001; Marconi & Hunt 2003; Graham 2007; Gültekin et al. 2009b).

Establishing an accurate $M_{\rm bh}$–L relation is beneficial for two reasons: first, to understand the physical basis as to why the relation exists and secondly, to provide a means for predicting SMBH masses for large samples of galaxies (e.g. Graham et al. 2007; Vika et al. 2009). Furthermore, active galactic nuclei (AGN) are the antecedent of most local inactive galaxies; studying the $M_{\rm bh}$–L relationship for both active and inactive galaxies can therefore provide information about the parallel evolution of black holes and their host galaxies. By exploring the origin of the scaling relation (Woo et al. 2006; Kim et al. 2008) at high redshift (Peng et al. 2006), and within active galaxies (McLure & Dunlop 2002; Bettoni et al. 2003; Gaskell & Kormendy 2009), one can study the evolution of SMBHs with time in comparison with the spheroid evolution. Bennert et al. (2010) found no change for evolution of the $M_{\rm bh}$–$L_{\rm tot}$ relation up to $z = 1$, in contradiction to the $M_{\rm bh}$–$L_{\rm sph}$ evolution. Further research of SMBH evolution shows that up to $z \sim 3$ host galaxies at fixed $M_{\rm bh}$ are less massive as compared to local galaxies (Treu et al. 2007; Jahnke et al. 2009). This indicates that SMBHs in early-type galaxies have reached their final mass during the very earliest phases of galaxy evolution (Ivanov & Alonso-Herrero 2003). As a result, the $M_{\rm bh}/M_{\rm gal}$ should be larger compared with the local ratio (Greene, Peng & Ludwig 2010), an outcome confirmed by

⋆E-mail: mv56@st-andrews.ac.uk

[1] Some other properties known to correlate with SMBH mass are the mean velocity dispersion (Tremaine et al. 2002) and the stellar mass (Häring & Rix 2004).

Table 1. Galaxy sample. Column (1): galaxy name; columns (2) and (3): equatorial coordinates (J2000); columns (4) and (5): K- and B-band magnitudes from the SIMBAD astronomical database; column (6): reddening estimate $E(B-V)$ from Schlegel, Finkbeiner & Davis (1998); column (7): Hubble type from NASA/IPAC Extragalactic Database (NED; and in bracket from GO11); column (8): redshift from the NED; column (9): activity (Sy: Seyfert, NLRG: narrow-line radio galaxy, H II: nuclear H II regions, L: low-ionization nuclear emission-line regions, LLAGN: low-luminosity AGN).

Galaxy name (1)	RA (J2000) (2)	Dec. (J2000) (3)	K (mag) (4)	B (mag) (5)	A_k (mag) (6)	Type (7)	Redshift (8)	Activity (9)
NGC 221	00 42 41.8	+40 51 57.2	5.09	9.2	0.057	cE2 (S0)	−0.0006	–
NGC 863	02 14 33.56	−00 46 00.0	9.54	14.0	0.013	SA(s)a	0.026 38	Sy1–2
NGC 1068	02 42 40.83	−00 00 48.4	5.79	9.7	0.012	SAb	0.003 79	Sy1–2
NGC 2778	09 12 24.35	+35 01 39.4	9.514	13.1	0.008	E (SB0)	0.006 83	–
NGC 2960	09 40 36.46	+03 34 36.6	9.783	13.6	0.016	Sa	0.016 45	Sy3
NGC 3245	10 27 18.52	+28 30 24.8	7.862	11.6	0.009	SA(r) (S0)	0.004 38	H II–L
NGC 4258	12 18 57.54	+47 18 14.3	5.464	9.6	0.006	SABbc	0.001 49	Sy1
NGC 4261	12 19 23.21	+05 49 29.7	7.26	12.0	0.006	E2	0.007 46	Sy3–L
NGC 4303	12 21 55.03	+04 28 28.7	6.843	10.9	0.008	SAB(rs)bc	0.005 22	H II–Sy2
NGC 4342	12 23 39.12	+07 03 12.9	9.023	13.0	0.008	SO	0.0025	–
NGC 4374	12 25 03.74	+12 53 13.1	6.222	10.8	0.015	E1	0.003 53	Sy2–L
NGC 4435	12 27 40.60	+13 04 44.4	7.297	11.9	0.011	SB(s) (SB0)	0.002 67	–
NGC 4459	12 29 00.13	+13 58 42.5	7.152	11.6	0.017	SA0	0.004 03	H II–L
NGC 4473	12 29 48.95	+13 25 46.1	7.157	11.2	0.010	E5	0.007 48	–
NGC 4486	12 30 49.42	+12 23 28.0	5.812	10.4	0.008	cD, E0	0.004 36	NLRG–Sy
NGC 4486a	12 30 57.89	+12 16 13.7	11.2	9.01	0.009	E2	0.000 50	–
NGC 4486b	12 30 31.82	+12 29 25.9	10.09	14.5	0.008	cE0	0.005 19	–
NGC 4552	12 35 40	+12 33 22	6.728	11.1	0.015	E1 (S0)	0.001 13	H II–Sy2–L
NGC 4564	12 36 27.01	+11 26 18.8	7.937	12.2	0.012	E6 (S0)	0.003 80	–
NGC 4596	12 39 56.16	+10 10 32.4	7.463	12.4	0.008	SB(r)0+	0.006 23	L
NGC 4621	12 42 02	+11 38 45	6.746	11.0	0.012	E5	0.001 37	–
NGC 4649	12 43 40.19	+11 33 08.9	5.739	10.3	0.010	E2	0.003 72	–
NGC 4697	12 48 35.7	−05 48 03	6.367	11.0	0.011	E6	0.004 14	LLAGN
NGC 5576	14 21 03.7	+03 16 16	7.827	11.9	0.011	E3	0.004 96	–
NGC 5813	15 01 11.3	+01 42 06	7.413	12.5	0.021	E1–2	0.006 58	L
NGC 5845	15 06 00.9	+01 38 01.4	9.112	13.8	0.020	E	0.004 83	–
NGC 5846	15 06 29.4	+01 36 19	6.935	11.9	0.020	E0	0.005 71	H II–L
NGC 7052	21 18 33.1	+26 26 48	8.574	14.0	0.046	E	0.0241	–
UGC 9799	15 16 44.6	+07 01 16.3	9.548	14.8	0.014	cD; E	0.0345	Sy2

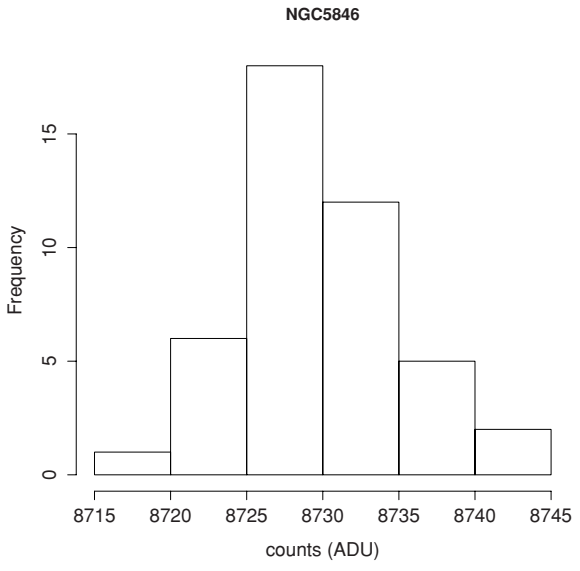

Figure 1. The distribution of the sky background for NGC 5846. The mean sky value is 8730 ADU with $\sigma = 6$.

quasi-stellar object observations up to $z \sim 6$ (Walter et al. 2004; Shields et al. 2006; McLeod & Bechtold 2009). However, other studies argue that this result may arise due to a selection bias (Borys et al. 2005; Alexander et al. 2008).

Another aspect of the M_{bh}–L relation is the behaviour at the low-luminosity end. Do SMBHs exist in low-mass galaxies (Merritt, Ferrarese & Joseph 2001) or is there a lower galaxy mass limit at which we can detect a SMBH? Hu (2009, hereafter H09) argue that bulgeless galaxies (or pseudo-bulges) follow a distinct relation, while Greene, Ho & Barth (2008) showed that a classical bulge is not necessary for a SMBH to exist. Pseudo-bulges are central components of late-type galaxies with disc features, and it is believed that they follow a separate formation path to the classical bulges with which they can coexist. For a review of the properties of pseudo-bulges, see Kormendy & Kennicutt (2004).

The first estimation of the M_{bh}–L relation in the near-IR was established by Marconi & Hunt (2003) using three band images from the Two Micron All Sky Survey (2MASS)[2] for a sample of 37 early- and late-type galaxies. The intrinsic scatter of their correlation ranges from ∼0.5 to ∼0.3 dex depending on the subsample selection. Graham (2007) refined the Marconi & Hunt (2003) M_{bh}–L relation by

[2] Jarrett et al. (2000).

using updated M_{bh} measurements and modifying the photometry of the data set and finding an intrinsic scatter of ∼0.30 dex.

More recently and in addition to the M_{bh}–L relation, Graham & Driver (2007, hereafter GD07, following on from Graham et al. 2001) found a relation between the galaxy light concentration n (Sérsic index) and M_{bh} with a comparable intrinsic scatter of 0.31 dex. In the review by Novak, Faber & Dekel (2006), the M_{bh}–n relation was shown to be as accurate on predicting M_{bh} as the M_{bh}–σ relations.

Graham et al. (2007) and Vika et al. (2009) applied both the M_{bh}–n and M_{bh}–L relations, respectively, to derive the nearby SMBH mass functions for the Millennium Galaxy Catalogue (Liske et al. 2003; Driver et al. 2005) and derived individual SMBH mass measurements for a sample of 1743 galaxies. While the mass functions agreed well within the cited errors, the comparison of the derived SMBH masses on a galaxy by galaxy basis showed a low consistency between the two predictors. They explained that the lack of correlation is in part due to the scatter introduced by combining elliptical and disc galaxies, the uncertainty of separating the bulge component from the disc component and due to the intrinsic scatter of the M_{bh}–L and M_{bh}–n correlations at optical wavelengths.

In this paper, we aim to reconstruct the M_{bh}–L and M_{bh}–n relations in the near-IR by using high-resolution United Kingdom Infrared Telescope (UKIRT) Infrared Deep Sky Survey (UKIDSS;

Table 2. Galaxy sample. The background is the mean value of 50 median sky values. Each median value has been estimated for a box of 100 pixel. The stddev is the standard deviation of the mean background value.

Galaxy name (1)	Seeing (pixel) (2)	Background (3)	stddev (4)	Exposure time (s) (5)	Survey (6)	Telescope/ instrument (7)
NGC 221	4.6	6540	8	10	SERV/1652	UKIRT/WFCAM
NGC 863	2.1	6606	3	10	LAS	UKIRT/WFCAM
NGC 1068	2.7	5945	5	10	LAS	UKIRT/WFCAM
NGC 2778	2.3	10723	1.2	10	B2	UKIRT/WFCAM
NGC 2960	1.9	4740	2	10	LAS	UKIRT/WFCAM
NGC 3245	1.9	10210	2	10	B2	UKIRT/WFCAM
NGC 4258	2.5	10635	2	10	B2	UKIRT/WFCAM
NGC 4261	1.4	5453	3	10	LAS	UKIRT/WFCAM
NGC 4303	1.7	6036	3	10	LAS	UKIRT/WFCAM
NGC 4342	1.1	5407	2	10	LAS	UKIRT/WFCAM
NGC 4374	2.8	5829	1.4	10	B2	UKIRT/WFCAM
NGC 4435	1.5	5782	5	10	LAS	UKIRT/WFCAM
NGC 4459	1.8	5402	3	10	LAS	UKIRT/WFCAM
NGC 4473	1.9	5368	4	10	LAS	UKIRT/WFCAM
NGC 4486	1.6	5580	9	10	LAS	UKIRT/WFCAM
NGC 4486a	1.2	5615	4	10	LAS	UKIRT/WFCAM
NGC 4486b	1.2	5581	5	10	LAS	UKIRT/WFCAM
NGC 4552	1.6	5612	4	10	LAS	UKIRT/WFCAM
NGC 4564	1.5	5123	4	10	LAS	UKIRT/WFCAM
NGC 4596	2.1	3316	2	10	LAS	UKIRT/WFCAM
NGC 4621	2.1	5117	3	10	LAS	UKIRT/WFCAM
NGC 4649	3.1	5258	5	10	LAS	UKIRT/WFCAM
NGC 4697	2.9	7449	3	10	B2	UKIRT/WFCAM
NGC 5576	2.6	5465	3	10	LAS	UKIRT/WFCAM
NGC 5813	1.9	7477	5	10	LAS	UKIRT/WFCAM
NGC 5845	2.0	8722	4	10	LAS	UKIRT/WFCAM
NGC 5846	1.8	8730	6	10	LAS	UKIRT/WFCAM
NGC 7052	2.1	6630	1.3	10	B2	UKIRT/WFCAM
UGC 9799	3.3	7377	2	10	LAS	UKIRT/WFCAM

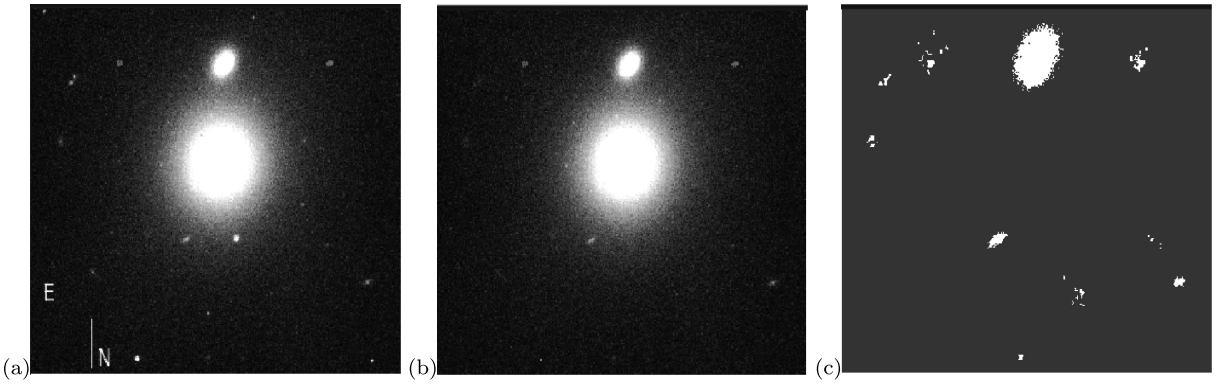

Figure 2. (a) *K*-band image of NGC 5846. (b) The same image cleaned of background stars. (c) The segmentation map. See Section 2 for details.

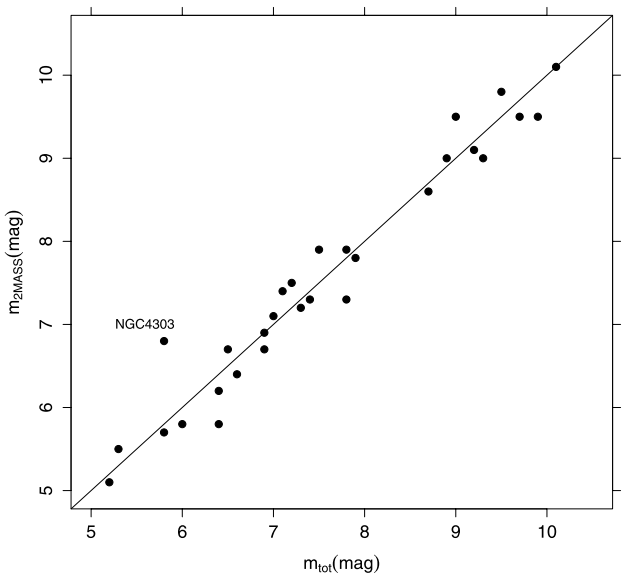

Figure 3. Correlation of this study's single Sérsic apparent magnitudes versus the 2MASS apparent magnitudes.

Lawrence et al. 2007) images which extend significant deeper ($\sim$2 mag arcsec^{-2}) than the previous studies based on 2MASS. We specifically choose near-IR photometry because galaxy profiles should be less perturbed by young star populations and by dust attenuation relative to optical passbands (Driver et al. 2008), thereby yielding a lower intrinsic scatter and enabling more accurate SMBH mass function determinations from the application of these relations to large surveys [e.g. Galaxy and Mass Assembly (GAMA); see Driver et al. 2009].

Section 2 describes the data selection and the data reduction. Section 3 describes the methodology for measuring 2D radial surface brightness profiles for our 29 galaxies using GALFIT3 (Peng et al. 2010) and presents information from the literature for our sample. In Section 4, we explore the M_{bh}–L and M_{bh}–n correlations and compare with previous studies. Finally, Section 5 summarizes our conclusions and suggests possible direction for further study.

2 DATA REDUCTION

We extract calibrated K-band images from UKIDSS for 29 galaxies for which SMBH masses have been measured. These galaxies are a subsample of the host galaxy population, where the mass of the SMBH has been measured using a direct method. The full sample consists of 86 galaxies with SMBHs and nine galaxies with intermediate massive black holes, as presented by GO11 and references therein.

The wide-field images were obtained using the Wide Field Infrared Camera (WFCAM) (Casali et al. 2007) on the 3.8-m UKIRT as part of the Large Area Survey UKIDSS-LAS (Lawrence et al. 2007). The pixel size of each detector is 0.4 arcsec with a gain of 4.5 e$^-$ ADU^{-1} and a read noise of 25 ADU.

The properties of our galaxy sample are listed in Table 1. We include galaxies with SMBH masses measured with stellar kinematics, gas kinematics, water masers, stellar proper motion and reverberation mapping (see Tables 6 and 7). The masses for NGC 2778, 4473, 4564, 4697 and 5845 have been modified from their initial published values due to an update of their distances (see GO11). Our sample includes 15 elliptical galaxies and 14 disc galaxies (see Table 1).

We also include for reference only the Milky Way parameters derived from other studies. In particular, the SMBH mass is $(4.3 \pm 0.3)10^6$ M$_\odot$ for a distance of 0.0083 Mpc (Gillessen et al. 2009), the bulge luminosity is $(4.0 \pm 1.2)10^8$ L$_\odot$ at 2.2 μm (Dwek et al. 1995) and the Sérsic index is $1.32^{+0.26}_{-0.22}$ (Kent, Dame & Fazio 1991; GD07).

2.1 Sky

The accuracy to which we can determine the sky background dictates the depth to which we can profile each galaxy. We measure the sky background by manually placing 40–50 boxes (10 × 10 pixel) at locations around each galaxy using the IRAF task `imexamine`. The sky value we then adopt is the mean of the median values from each box (see Fig. 1 for details). The boxes are selected to lie away from stars, the faint halo of the galaxy, neighbouring galaxies that may exist and to be uniformly distributed around each image.

Some images (NGC 2778, 3245, 4258 and 7052) have a noticeable background gradient. We correct the gradient with the use of a SExtractor (Bertin & Arnouts 1996) fully resolved background map. To ensure that the subtraction of the background map will not deteriorate the galaxy flux, we first subtract the galaxy with the help of a model constructed with IRAF - `ELLIPSE BMODEL`. After we have removed the model, we create a fully resolved background map which we subtract from the initial image. The sky background values derived from the method described above can be found in Table 2 and are used later as an input to GALFIT3. All background values have been independently checked using STARLINK - `ESP - HISTPEAK` and agree within the quality errors. Nevertheless, we do note in particular the extensive structure in the background of NGC 4486 possibly due to the UKIDSS reduction pipeline. The NGC 4486 case will be discussed further in Section 4.4.

2.2 PSF

Two point spread functions (PSFs) are created for each galaxy, based on stars taken from the same data frame and using the package IRAF DAOPHOT. The PSF model is described by a penny2 function. Penny2 has a Gaussian core and Lorentzian wings which are free to be tilted in different directions. We construct the PSF from a sample of 10–15 stars selected from each galaxy/image in interactive mode. A different set of stars is used for each PSF. Saturated stars, or stars very close to the galaxy with unclear background levels, are excluded from the sample. After the creation of the DAOPHOT PSF, we use it to subtract all stars from the original image. The left-hand panel and the middle panel of Fig. 2 show an example galaxy image before and after removing the stars.

2.3 Image masks

In some images, the main galaxy is surrounded by satellite galaxies (e.g. UGC 9799), bad pixels and saturated stars (e.g. NGC 4459). The light distribution from the neighbouring galaxies and the area that the bad pixels cover cannot be cleaned with the same technique we used for the stars. In these cases, we use an image mask that indicates to GALFIT3 which areas of the image should not be used. We create these maps using SExtractor segmentation maps. The right-hand panel of Fig. 2 shows the SExtractor segmentation maps with

pixels having a non-zero value in the map being excluded from the fitting process.

3 PHOTOMETRIC DECOMPOSITION

We obtained the structural parameters of the host galaxies by performing 2D fitting with GALFIT3 (Peng et al. 2010). GALFIT3 constructs analytic fits to galaxy images, allowing multicomponent functions representing bulge, disc, bar, point-source and sky background components. GALFIT3 uses the Levenberg–Marquardt technique to find the best fit. GALFIT3 algorithm uses this non-linear least-squares technique to minimize the χ^2 residual between the galaxy image and the model by modifying all the free parameters and accepting them when the χ^2 is reduced. The normalized χ^2 is

Table 3. GALFIT3-derived parameters. Column (1): name of the galaxy; columns (2–4): the spheroid apparent magnitude, effective radius along the semimajor axis and Sérsic index; columns (5–6): the disc apparent magnitude and scalelength; columns (7–9): the bar apparent magnitude, effective radius and Sérsic index; columns (10–11): the spheroid and total absolute magnitude; column (12): the best fit chosen.

Galaxy name (1)	m_{sph} (mag) (2)	r_{eff} (arcsec) (3)	n_{sph} index (4)	m_d (mag) (5)	r_s (arcsec) (6)	m_{bar} (mag) (7)	r_{bar} (mag) (8)	n_{bar} index (9)	M_{sph} (mag) (10)	M_{tot} (mag) (11)	Best fit (12)
NGC 221	$6.5^{+0.88}_{-0.02}$	18.3	$2.1^{+0.01}_{-1.28}$	5.8	43.7	–	–	–	−18.2	−19.5	Bulge+disc+mask centre
NGC 863	$10.9^{+0.2}_{-0.32}$	1.66	$2.6^{+0.83}_{-0.001}$	10.8	6.5	–	–	–	−18.4	−19.7	Bulge+disc+psf
NGC 1068	$8.2^{+0.01}_{-0.08}$	2.8	$0.8^{+0.03}_{-0.02}$	6.5	16.7	7.9	11.8	0.3	−22.7	−24.9	Bulge+disc+bar+mask centre
NGC 2778	$10.9^{+0.96}_{-0.13}$	1.5	$2.7^{+0.04}_{-2.53}$	10.7	5.4	–	–	–	−20.8	−21.9	Bulge+disc
NGC 2960	$10.8^{+0.26}_{-0.09}$	1.8	$4.0^{+0.46}_{-0.98}$	10.7	6.8	–	–	–	−23.5	−24.8	Bulge+disc
NGC 3245	$9.0^{+0.2}_{-0.08}$	3.5	$2.6^{+0.14}_{-0.36}$	8.3	20.5	–	–	–	−22.6	−24.1	Bulge+disc
NGC 4258	$7.8^{+0.17}_{-0.08}$	17.0	$3.5^{+0.34}_{-0.11}$	6.7	50.2	–	–	–	−21.5	−24	Bulge+disc+psf
NGC 4261	$7.3^{+0.06}_{-0.1}$	24.2	$3.5^{+0.19}_{-0.27}$	–	–	–	–	–	−25.2	−25.2	Elliptical+mask centre
NGC 4303	$9.5^{+0.03}_{-0.01}$	2.8	$0.9^{+0.01}_{-0.05}$	7.5	30.0	9.1	49.5	0.5	−21.6	−25.2	Bulge+disc+bar+psf
NGC 4342	$10.3^{+0.008}_{-0.004}$	0.86	$1.9^{+0.02}_{-0.001}$	9.6	5.1	–	–	–	−20.9	−22.3	Bulge+disc
NGC 4374	$6.4^{+0.02}_{-0.01}$	28.7	$3.5^{+0.02}_{-0.03}$	–	–	–	–	–	−24.9	−24.9	Elliptical+mask centre
NGC 4435	$8.8^{+0.03}_{-0.08}$	4.5	$1.5^{+0.05}_{-0.05}$	8.7	18.9	9.9	20.8	0.3	−22	−22.9	Bulge+disc+bar
NGC 4459	$7.2^{+0.11}_{-0.14}$	25.0	$3.9^{+0.54}_{-0.53}$	–	–	–	–	–	−23.8	−24.1	Elliptical+moffat core
NGC 4473	$7.2^{+0.11}_{-0.07}$	21.3	$4.3^{+0.43}_{-0.45}$	–	–	–	–	–	−23.7	−23.7	Elliptical+mask centre
NGC 4486	$6.0^{+0.45}_{-0.2}$	34.6	$2.4^{+0.54}_{-1.68}$	–	–	–	–	–	−25.0	−25.0	Elliptical+mask centre
NGC 4486a	$9.3^{+0.12}_{-0.14}$	8.1	$2.0^{+0.28}_{-0.72}$	–	–	–	–	–	−21.9	−21.9	Elliptical+mask centre
NGC 4486b	$10.0^{+0.12}_{-0.13}$	2.6	$3.2^{+0.12}_{-0.1}$	–	–	–	–	–	−21.2	−21.2	Elliptical
NGC 4552	$6.9^{+0.05}_{-0.11}$	16.7	$3.6^{+0.31}_{-0.33}$	–	–	–	–	–	−24.0	−24.0	Elliptical
NGC 4564	$9.4^{+0.06}_{-0.01}$	3.0	$3.7^{+0.1}_{-0.24}$	–	–	8.6	23.4	1.3	−21.4	−23.1	Bulge+disc
NGC 4596	$8.3^{+0.14}_{-0.05}$	13.2	$3.6^{+0.08}_{-0.25}$	8.6	44.7	9.1	37.9	0.4	−22.9	−24	Bulge+disc+bar
NGC 4621	$6.5^{+0.09}_{-0.1}$	54.7	$5.7^{+0.22}_{-0.41}$	–	–	–	–	–	−24.8	−24.8	Elliptical+mask centre
NGC 4649	$5.7^{+0.19}_{-0.14}$	45.7	$3.6^{+0.54}_{-0.75}$	–	–	–	–	–	−25.4	−25.4	Elliptical+mask centre
NGC 4697	$6.6^{+0.01}_{-0.03}$	39.1	$3.8^{+0.03}_{-0.01}$	–	–	–	–	–	−20.3	−20.3	Elliptical
NGC 5576	$7.8^{+0.24}_{-0.17}$	16.9	$5.1^{+1.06}_{-1.94}$	–	–	–	–	–	−24.2	−24.3	Elliptical+mask centre
NGC 5813	$6.7^{+0.66}_{-0.65}$	132.9	$8.3^{+2.55}_{-2.69}$	–	–	–	–	–	−25.9	−25.9	Elliptical+mask centre
NGC 5845	$9.2^{+0.01}_{-0.02}$	3.5	$2.6^{+0.07}_{-0.06}$	–	–	–	–	–	−22.8	−22.9	Elliptical
NGC 5846	$6.8^{+1.07}_{-0.33}$	46.3	$3.7^{+1.07}_{-5.29}$	–	–	–	–	–	−25.2	−25.1	Elliptical+mask centre
NGC 7052	$10.0^{+0.03}_{-0.07}$	4.3	$1.8^{+0.08}_{-0.01}$	9.2	15.2	–	–	–	−24.2	−25.6	Bulge+disc
UGC9799	$9.4^{+0.48}_{-0.26}$	31.3	$2.9^{+0.41}_{-0.96}$	–	–	–	–	–	−26.4	−26.8	Elliptical+mask centre

Table 4. Second better fit chosen. The layout is as in Table 3.

Galaxy name (1)	m_{sph} (mag) (2)	r_{eff} (arcsec) (3)	n_{sph} index (4)	m_d (mag) (5)	r_s (arcsec) (6)	m_{bar} (mag) (7)	r_{bar} (mag) (8)	n_{bar} index (9)	M_{sph} (mag) (10)	M_{tot} (mag) (11)	Best fit (12)
NGC 4258	$8.8^{+0.2}_{-0.09}$	6.3	$2.2^{+0.4}_{-0.12}$	6.6	50.0	8.9	0.9	22.0	−20.5	−24	Bulge+disc+bar+psf
NGC 4374	$7.6^{+0.04}_{-0.03}$	7.8	$1.6^{+0.02}_{-0.04}$	7.0	22.8	–	–	–	−23.7	−24.9	Bulge+disc
NGC 4435	$8.8^{+0.02}_{-0.07}$	4.5	$1.5^{+0.04}_{-0.03}$	8.6	17.4	9.8	0.4	19.9	−21.9	−22.9	Bulge+disc+bar+psf
NGC 4486b	$11.2^{+0.11}_{-0.1}$	0.9	$1.8^{+0.15}_{-0.11}$	10.7	2.2	–	–	–	−20.0	−21.2	Bulge+disc
NGC 4697	$7.9^{+0.01}_{-0.03}$	10.0	$2.9^{+0.03}_{-0.01}$	7.2	23.8	–	–	–	−22.4	−20.3	Bulge+disc
NGC 7052	$8.6^{+0.04}_{-0.06}$	18.8	$3.5^{+0.05}_{-0.01}$	–	–	–	–	–	−25.6	−25.6	Elliptical+mask centre

in the form

$$\chi^2 = \frac{1}{n}\sum_{1}^{nx}\sum_{1}^{ny}\frac{[f_d(x, y) - f_m(x, y)]^2}{\sigma(x, y)^2}, \quad (1)$$

where n is the number of degrees of freedom in the fit, nx and ny are the x and y image dimensions, $f_d(x, y)$ is equal to the image flux at pixel (x, y) and $f_m(x, y)$ is the sum of all the functions of flux at the same pixel. The term $\sigma(x, y)$ is the Poisson error at each pixel position. The $\sigma(x, y)$ value can be estimated internally by GALFIT3 based on the gain and read-noise values found in the header of each galaxy image or provided separately as a FITS image. Pixels contained in the mask image are not included in the χ^2 calculation.

The background is kept fixed to the value derived in Section 2.1. GALFIT3 convolves the model with the PSF (see Section 2.2) to account for the results of atmospheric seeing. The free parameters for each component are the magnitude, the scalelength (r_s)/effective radius (r_e), the concentration index n for the Sérsic models (Sérsic index), the axial ratio and the position angle.

We modelled the radial light distribution of each galaxy using combinations of the following analytic functions: a Sérsic function (see equation 2) to model elliptical galaxies, the bulge and/or the bar of lenticular and spiral galaxies; an exponential function (equation 2, where $n = 1$) to model the disc of the galaxy and a Moffat function to model/mask the central part of one elliptical galaxy. For some barless disc galaxies, the combination of a Sérsic plus an exponential component was insufficient to model the galaxy. In these cases, we modelled the galaxies with a combination of two Sérsic functions. The Sérsic (1968) function is given by

$$I(r) = I_e \exp\left\{-b_n\left[\left(\frac{r}{r_e}\right)^{1/n} - 1\right]\right\}, \quad (2)$$

where I_e is the intensity at the effective radius (r_e), n is the Sérsic index and b_n is a function of n. The value of b_n can be derived from $\Gamma = 2\gamma(2n, b_n)$ and is used so that the effective radius encloses half of the total luminosity (see Graham & Driver 2005). When the Sérsic index is fixed to $n = 4$, 1 or 0.5, the Sérsic profile is identical to the well-known de Vaucouleurs, exponential or Gaussian profile, respectively.

For the first run of GALFIT3, we performed a single Sérsic model fit for all galaxies assuming that we can describe the distribution of light with a single component. The first run used initial values for the free parameters as implied by SExtractor. The magnitudes derived from the single Sérsic model were compared with the 2MASS magnitudes. The 2MASS magnitudes agreed with our single component magnitudes except for two galaxies, NGC 4343 and 4486A (see Fig. 3). For those cases where an additional component was required, either due to a poor Sérsic fit or an obvious disc in the images, a second run was conducted. The output parameters of the first run were then used as input parameters for the second run of GALFIT3. The second run used a two-component model (i.e. Sérsic bulge–exponential disc) for disc galaxies. The Sérsic bulge plus exponential disc model for the lenticular galaxy NGC 4564 was still deficient, and so a double Sérsic model was adopted for a third run. Note that the resulting Sérsic index for the disc of this galaxy was found to be 1.3 which is plausibly close to the value of the exponential function ($n = 1$).

In one case, the disc galaxy NGC 4459, the Sérsic plus disc fit was not sufficient to model the galaxy. After trying to model the galaxy by applying a single Sérsic model or combining extra functions, we conclude that NGC 4459 can been modelled better with a combination of a Sérsic function and a Moffat function. The Moffat function in GALFIT3 has five free parameters: the total magnitude, the full width at half-maximum (FWHM), the β power law, the axial ratio and the position angle. We fixed the FWHM and the β parameter to values that we derived through the IRAF task `psfmeasure`.

As described above, the outputs of the second run were used as input for the third run for galaxies whose residuals implied the existence of a bar. We applied a third run to galaxies with a bar component by using a three-component model, i.e. Sérsic bulge–exponential disc–Sérsic bar.

An additional run was also applied to active galaxies (as indicated by X-ray or radio observations) that have a bright nucleus in near-IR (corresponding to a point source at our resolution). These galaxies are NGC 863, 4258, 4303 and 4435. In these cases, we model the nucleus as a PSF. It is not always clear whether introducing the PSF component improves the model or not, and for this reason we provide two models for some active galaxies, one with and one without the PSF. Table 3 lists the main profile for each galaxy, which is used to derive the M_{bh}–L and M_{bh}–n relations, while Table 4 shows the alternative profile information.

Table 5. Mask size of the inner regions for the galaxies for which their profile deviates from the Sérsic model. In the case of NGC 1068, the saturated AGN has been masked, while in the case of the NGC 4486A, the central area of the galaxy has been masked due to the existence of a bright star.

Galaxy name (1)	Mask (arcsec) (2)	Mask/r_{eff} (3)
NGC 221	2.75	15 per cent
NGC 1068	0.6	Saturated area
NGC 4261	1.0	4 per cent
NGC 4374	1.0	3 per cent
NGC 4473	1.4	6 per cent
NGC 4486	3.8	10 per cent
NGC 4486A	∼5	Saturated area
NGC 4621	1.8	3 per cent
NGC 4649	2.6	5.6 per cent
NGC 5576	2.0	11 per cent
NGC 5813	1.0	1 per cent
NGC 5846	2.6	5.6 per cent
UGC 9799	1.0	3 per cent

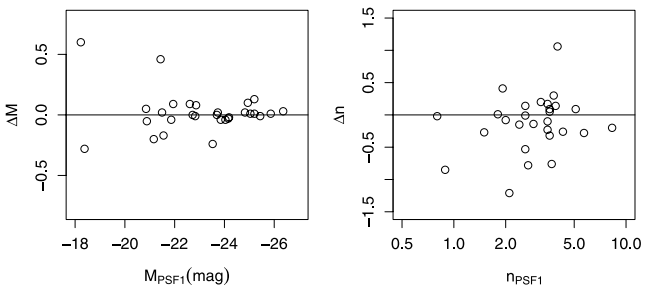

Figure 4. Left-hand panel: correlation of the spheroid absolute magnitudes of the best fit for two different PSFs. Right-hand panel: the same as the left-hand panel for Sérsic indices. The black line in both panels is the one to one relation.

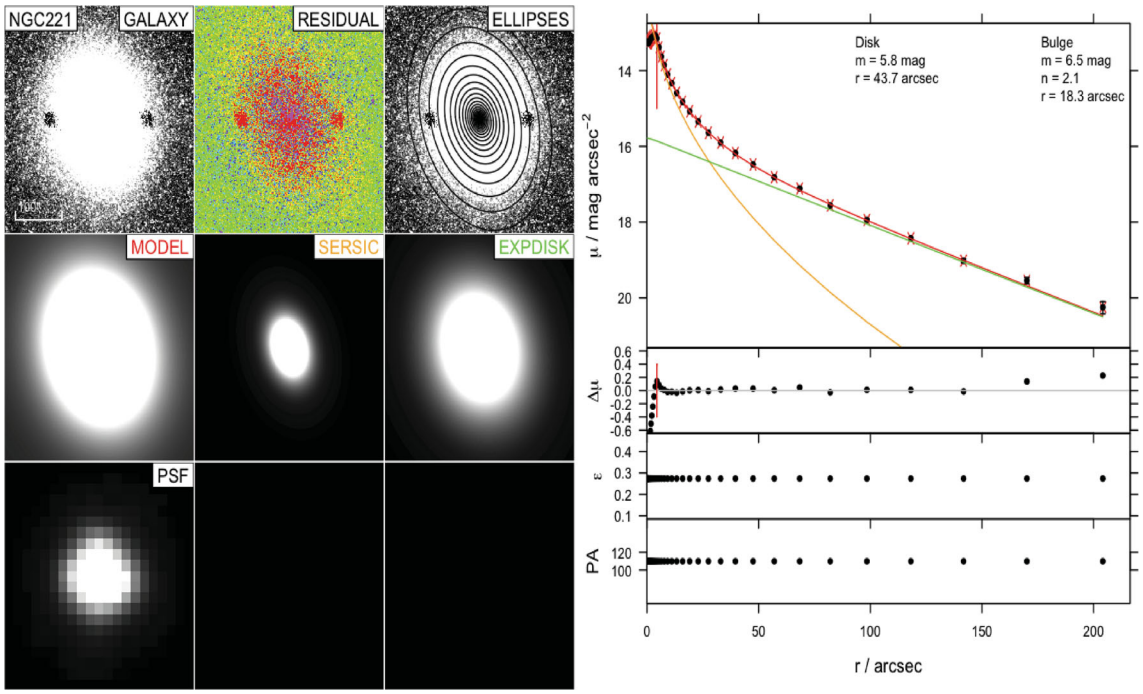

Figure 5. 2D decomposition for NGC 221. Left-hand panels: we display the original image, the residuals, the original image with IRAF ELLIPSE ellipses on top, the final model, the subcomponents and the PSF which GALFIT3 used to convolve the original image. Right-hand panels: from top to bottom, surface brightness μ, the deviation of the galaxy surface brightness (red line) from the model surface brightness, the ellipticity ϵ and the position angle PA of the bulge. The black circles indicate the surface brightness profiles of the original image, while the red line the surface brightness from the model as ellipse measures them. The rest of the lines correspond to each of the subcomponents. The colour of each line corresponds to the colour of the legend found on the left-hand panel. The black line error bars show the uncertainty of estimating the surface brightness due to uncertainty of measuring the sky value. The red line error bars indicate the uncertainty of IRAF ELLIPSE to measure the surface brightness. The red vertical line indicates the use of a mask that prevents GALFIT3 from profiling the core of the galaxy. See the properties of the fitting components in Table 3.

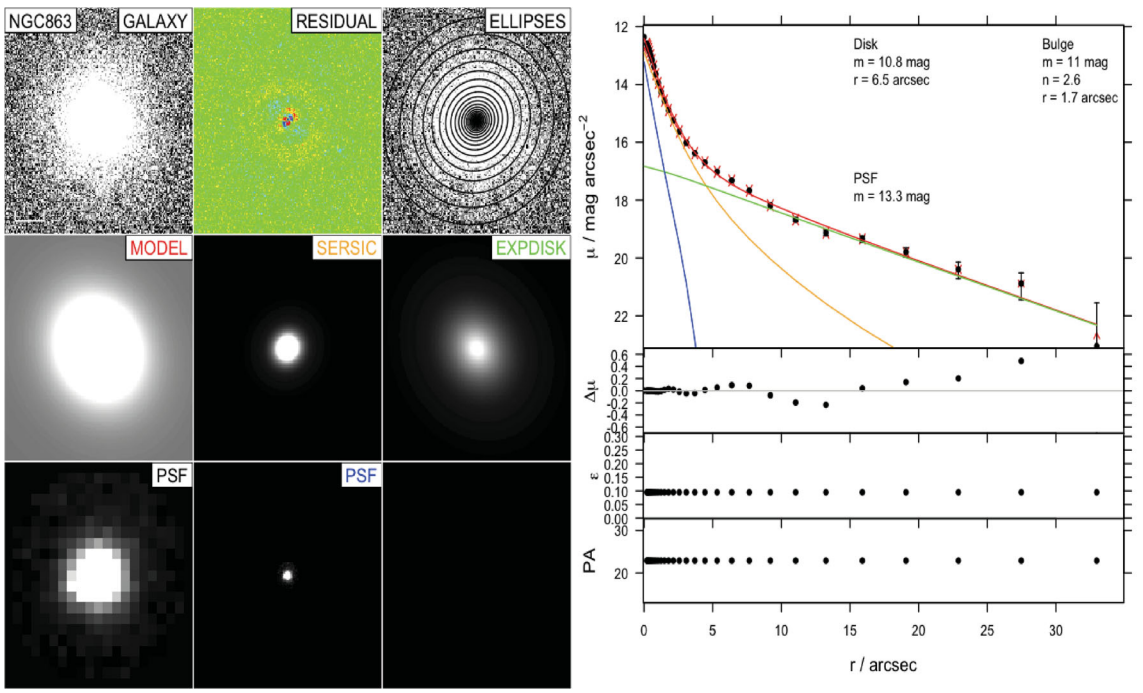

Figure 6. NGC 863 has been classified as a spiral galaxy. The layout is as in Fig. 5.

Massive elliptical and bulge galaxies often exhibit partially depleted cores (i.e. deviations of the profile in the inner regions), this phenomena is well known, and the innermost regions (1–5 per cent of the effective radius) often deviate (see e.g. Kormendy et al. 2009; Glass et al. 2011). While there is relatively little flux involved, their presence can cause particular difficulties in measuring an accurate Sérsic index. In Section 3.2, we present different methods used by previous studies to fit the core galaxies. GALFIT3 does not provide a function to model the depleted cores, but if we ignore the existence of the core structure and model the core galaxies with a single Sérsic model we will erroneously weight the fit to model the inner high signal-to-noise ratio core. In these galaxies where the original profiles showed distinct departures in the inner regions, we elect to mask. For these systems, indicated in Table 5, we implement a mask and re-profile and gradually increase the mask size until a stable outcome is found. Table 5 column 3 shows the final mask

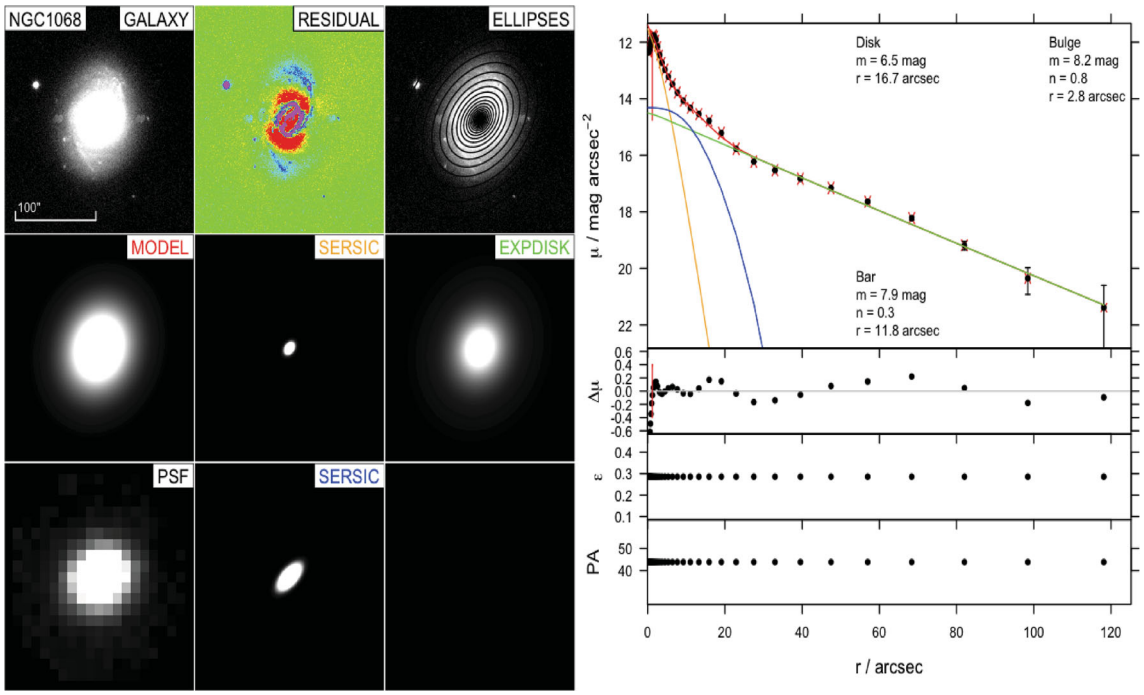

Figure 7. At the nuclei of the galaxy arises an artificial drop of counts. To prevent GALFIT3 profiling this inner part, we masked the nuclei with a box of 1.5 arcsec^2. The layout is as in Fig. 5.

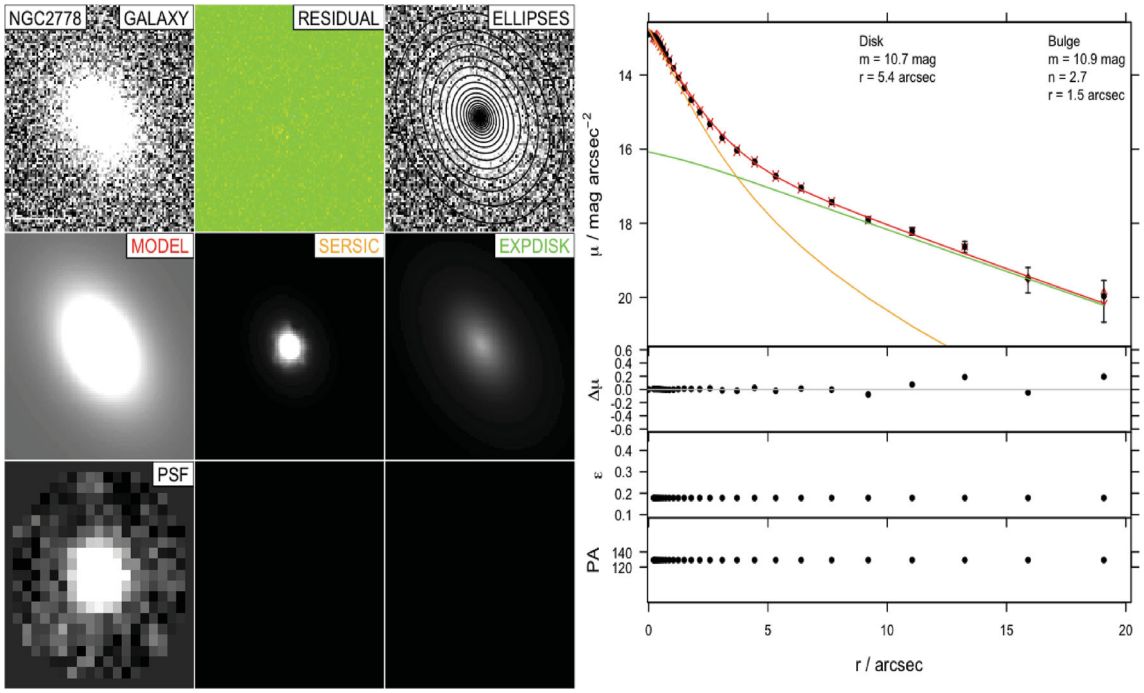

Figure 8. The surface brightness profile for NGC 2778. The layout is as in Fig. 5.

sizes in units of the effective radius for each of our galaxies, and no obvious correlation or rule of thumb is seen. We conclude that masking is critical for the recovery of an accurate Sérsic index but actually affects the bulge luminosity relatively little as the majority of the flux lies outside the core region. Also, in the case of some bright galaxies, the centre of the galaxy has been saturated, and as a result an artificial drop of counts appears. Here too, we overcome the problem of the saturated area by masking the data. The galaxies to which a core mask has been applied are NGC 1068, 221, 4261, 4374, 4473, 4486, 4486A, 4621, 4649, 5576, 5813 and 5846, and UGC 9799.

When the minimization is complete, GALFIT3 produces FITS files for the original image, the model, the residual and the individual images for each component. To visually examine the goodness of the fit, we use IRAF ELLIPSE to produce a 1D profile of the input galaxy, the fit and the each subcomponent. This process ensures

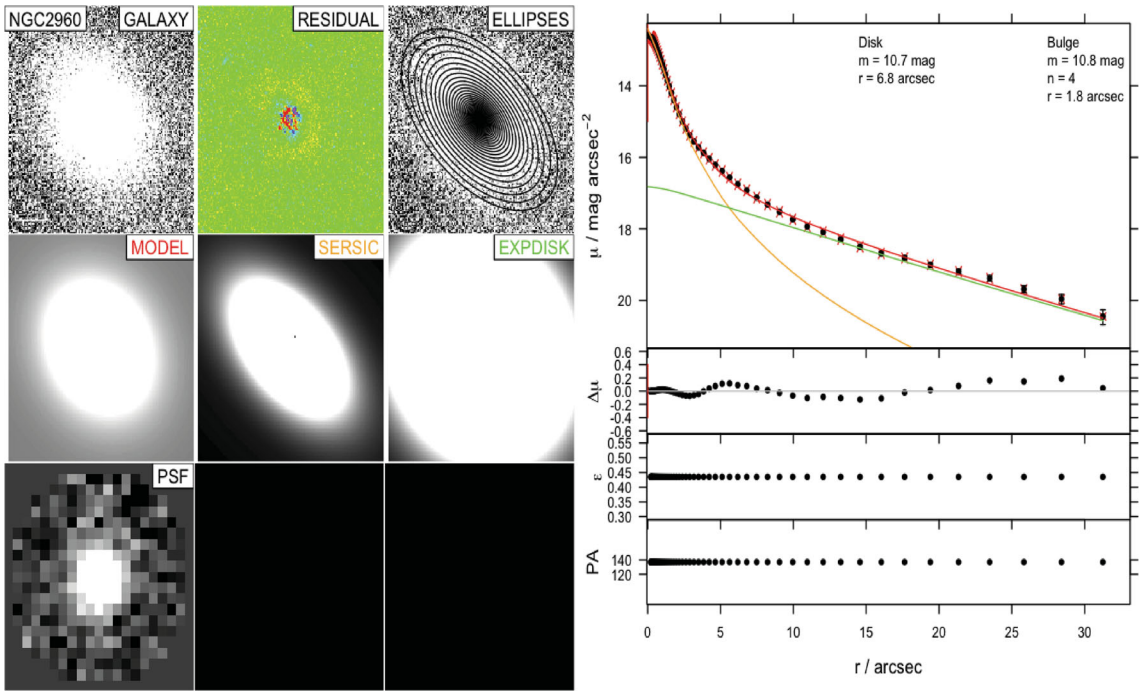

Figure 9. The location of the galaxy on the image does not permit GALFIT3 to profile the galaxy further than 35 arcsec. However, even under this limitation, GALFIT3 output look to be realistic, so we trust the bulge properties. The layout is as in Fig. 5.

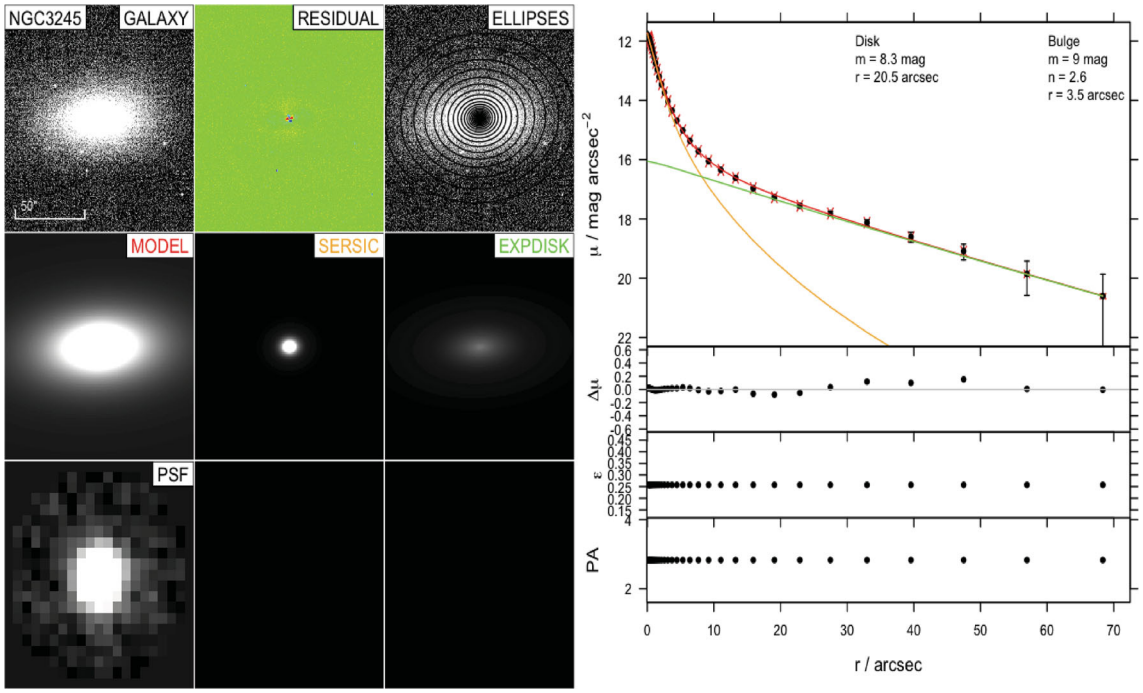

Figure 10. GALFIT3 results are in agreement with the kinematic studies that show existence of disc. The layout is as in Fig. 5.

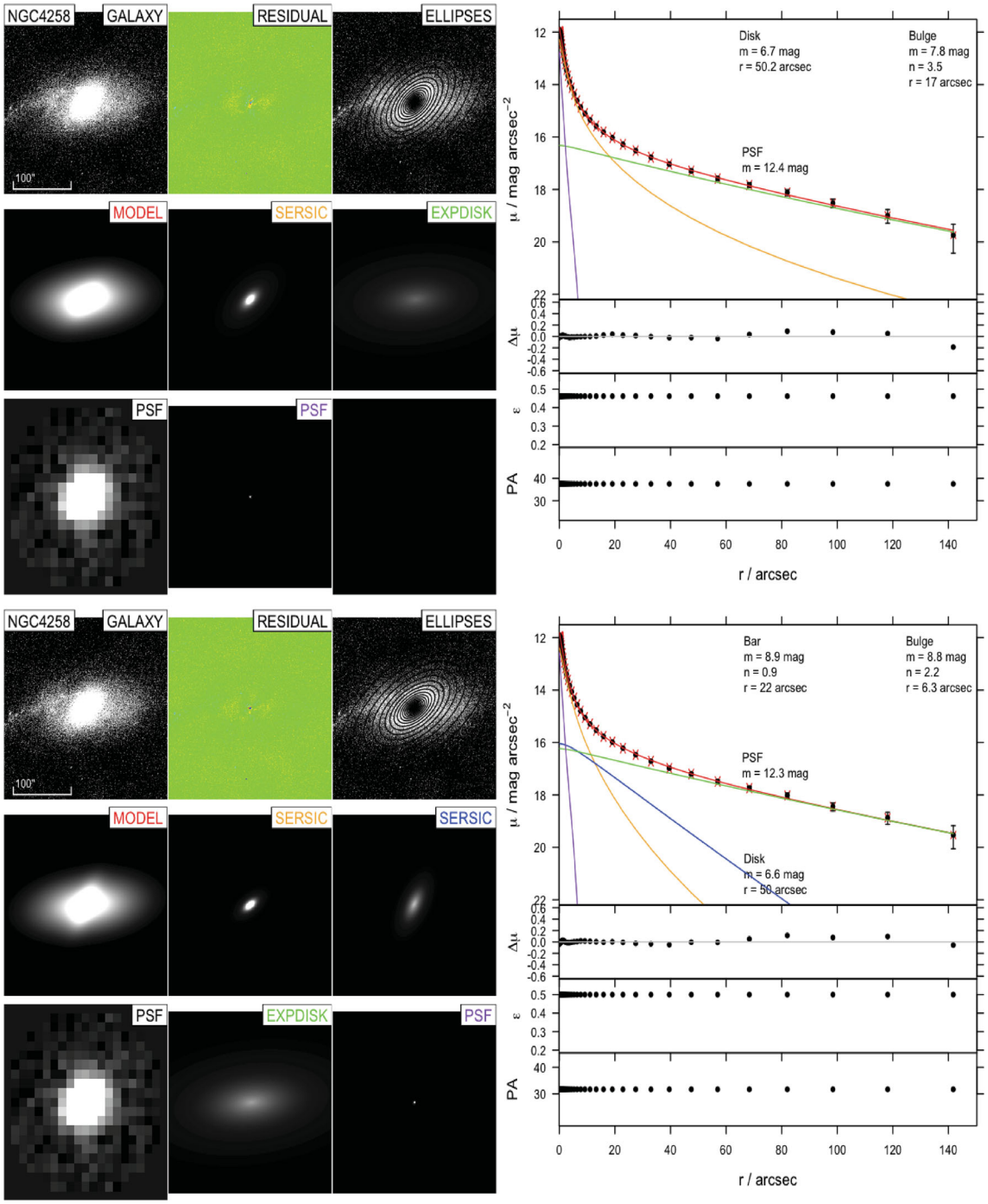

Figure 11. The surface brightness profile for NGC 4258 for two different fits: (a) Sérsic + exponential model + PSF nuclei and (b) double Sérsic + exponential model + PSF nuclei. The layout is as in Fig. 5.

that the data and models are inspected in an identical manner with the position angle, and the axial ratio of the ellipses were fixed to the values that GALFIT3 has estimated for the bulge/spheroid. We placed the resulting ellipses on to both the model image and the subcomponent images of the model. With this test, we can see if the azimuthally measured surface brightness along the major axis of the model is in agreement with the surface brightness profile of the galaxy, and also the contribution to the overall profile from each component. The derived surface brightness profiles are displayed in Figs 5–33 together with the image of the galaxy, the residual, the model, the subcomponents and the PSF as indicated. It is important to stress that these profiles are *not* an output of GALFIT3 but simply an inspection tool that processes the original image and GALFIT3 output in an identical manner.

The apparent magnitudes produced by GALFIT3 are converted into absolute magnitudes using the values of distance (d) and extinction (A_k) as listed in Tables 1 and 6, respectively.

The faint limit in surface brightness to which our fits are deemed reliable varies for each image from 20.6 to 22.7 mag arcsec^{-2}. Five galaxies (NGC 221, 2960, 4473, 4621 and UGC 9799) in our sample

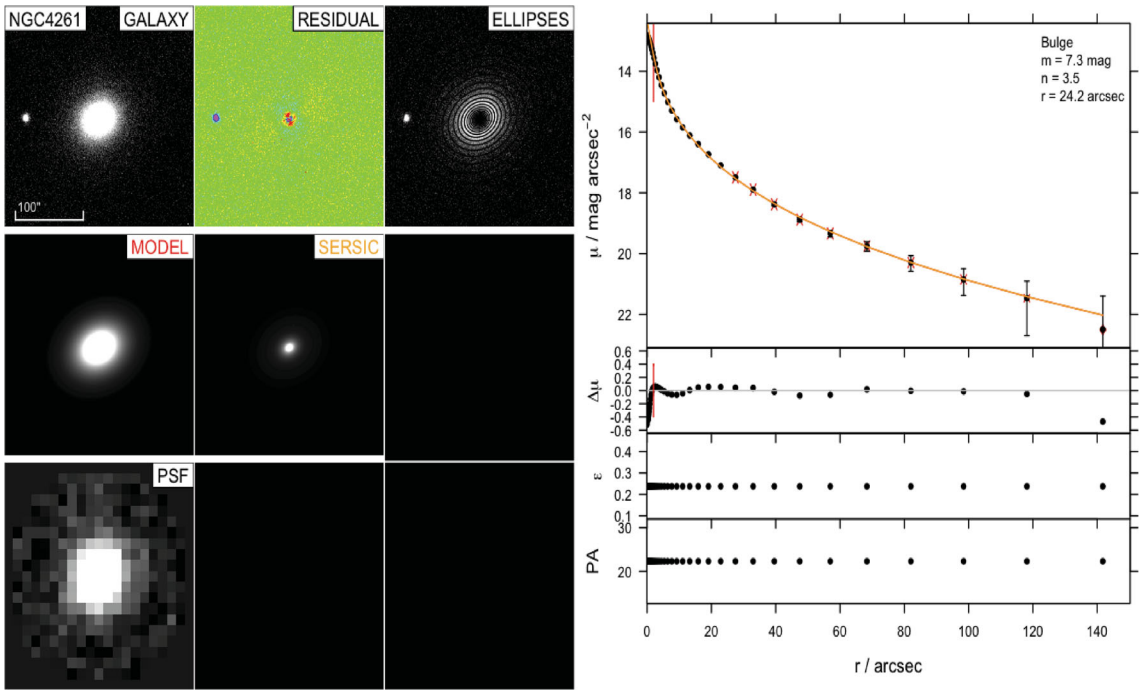

Figure 12. For NGC 4261 galaxy, GALFIT3 generates low Sérsic index model compared to the 1D pre-existing models (see Subsection 3.2). We masked the inner 2 arcsec. The layout is as in Fig. 5.

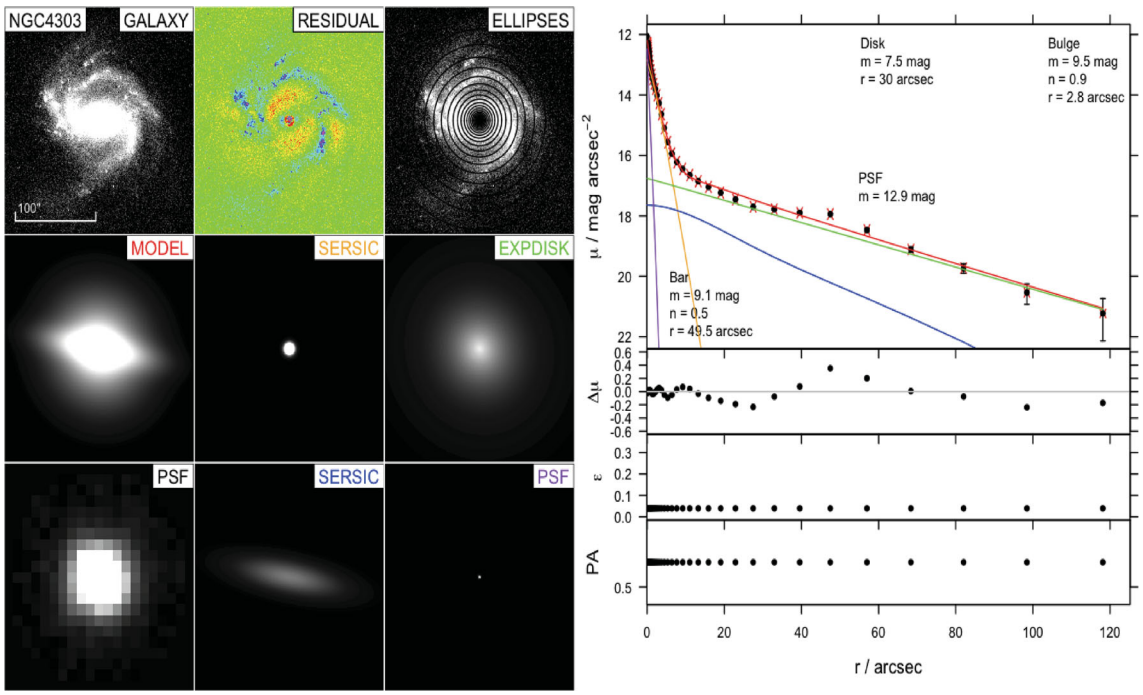

Figure 13. The surface brightness profile for NGC 4303. The layout is as in Fig. 5.

are located at the edge of their cut-out. These galaxies cannot be profiled 'down to their faint surface brightness limit'. After testing the model surface brightness profile with IRAF ELLIPSE following the method described above for these five galaxies, we decided that their derived parameters are robust (see Figs 5, 9, 18, 25 and 33).

3.1 Uncertainties

As we described in Section 2.1, we measured the background sky value as accurately as the image quality allows. However, small variances on the mean sky value can significantly modify the output values. To calibrate the errors due to sky uncertainty we re-run

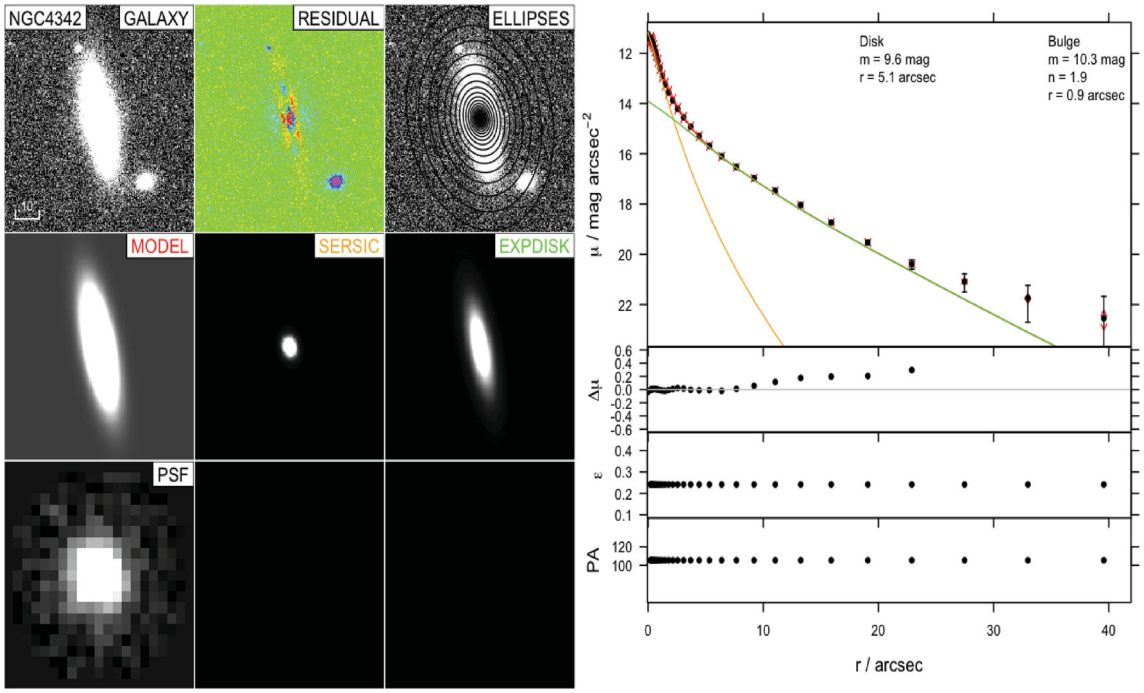

Figure 14. The layout is as in Fig. 5. IRAF ELLIPSE outer ellipses are contaminated with extra light from the satellites; as a result, the model surface brightness mismatches the IRAF ELLIPSE points.

GALFIT3 using the best-fitting values but changing the mean sky level by $\pm 1\sigma$ (where σ is the uncertainty to which the mean sky level is known and listed in column 4 of Table 2). These two additional runs provide us with 1σ uncertainties for the magnitudes and the Sérsic indices required for deriving robust M_{bh}–L and M_{bh}–n relations (see Section 4.1).

The dominant systematic uncertainty is the validity of the choice of function(s) to describe the light distribution of a galaxy. Most galaxies in our sample leave residual structures after removing the model, which may indicate smaller components that have not been modelled. In those cases where we see ambiguity, we refit with/without the ambiguous component and report for completeness the alternative results in Table 4.

Finally, we test the uncertainty introduced by the PSF. To explore this, we re-run GALFIT3 using the best-fitting values but changing the PSF that GALFIT3 use for convolution (see Fig. 4 and Section 2.2). We find that the uncertainty introduced by the PSF ($\Delta M = 0.02$, $\Delta n = 0.2$) is small compared with the sky value uncertainty.

3.2 Notes on modelling for individual galaxies

NGC 221 (M32), M31's closest, satellite has a contaminated brightness profile due to the M31 disc. The contaminated light has a gradient from north-west, where it takes the maximum value, to south-east. Previous studies have excluded the inner 10 arcsec from their studies (Kent 1987; Choi, Guhathakurta & Johnston 2002; Graham 2002). Graham (2002) found that NGC 221 can be best profiled with a bulge/disc model ($n_{bulge} = 1.51$), while H09 found $n_{bulge} = 4.00$ plus disc.[3]

NGC 863 (Mrk 590) is a Seyfert 1 galaxy with a broad-line spectrum.

NGC 1068 (M77) is one of the most well-studied barred spiral galaxies. The main bar was first observed in the near-IR by Scoville et al. (1988), while other studies have observed multiple bars (e.g. Erwin 2004). The nucleus hosts a Seyfert1–2 source with double jet observed in the radio (Gallimore et al. 1996) making the mid- and near-IR nuclei (inner 4 arcsec) appear extremely red (Alonso-Herrero et al. 1998; Bock et al. 2000). Drory & Fisher (2007) identify the existence of a pseudo-bulge based on the nuclear structure of the galaxy. H09 found $n_{bulge} = 1.51$, $n_{bar} = 0.7$ plus an exponential disc.

NGC 2778 has been classified as an elliptical galaxy, but GD07[4] showed that it can be described better with a Sérsic bulge $n_{bulge} = 1.6$ plus an exponential disc which indicates a lenticular galaxy. This conclusion is also supported from kinematical studies (Rix, Carollo & Freeman 1999).

NGC 2960 (Mrk 1419) – no previous information.

NGC 3245 – kinematical studies show circularly rotating disc (Walsh et al. 2008). H09 found $n_{bulge} = 3.9$ plus an exponential disc.

NGC 4258 (M106) is a barred-spiral Seyfert galaxy that has been studied extensively over a broad-band of wavelengths. The nucleus contains an edge-on warped accretion disc with radio jet (Herrnstein et al. 1997) and strong maser emission (Claussen, Heiligman & Lo 1984). Both GD07 and H09 used a bulge/disc model and found $n_{bulge} = 2.04$ and 2.6, respectively. Fisher & Drory (2010) found that $n_{bulge} = 2.8$ in mid-IR and presented evidence of pseudo-bulge characteristics.

NGC 4261 is the main elliptical galaxy in a group of 33 galaxies located behind the Virgo cluster (Huchra et al. 1983). The

[3] H09 use the 2D bulge/disc decomposition program BUDDA and K-band images, while Graham (2002) use the 1D algorithm UNCMND and R-band images.

[4] GD07 derive their major axis surface brightness profiles via fitting elliptical isophotes using IRAF ELLIPSE.

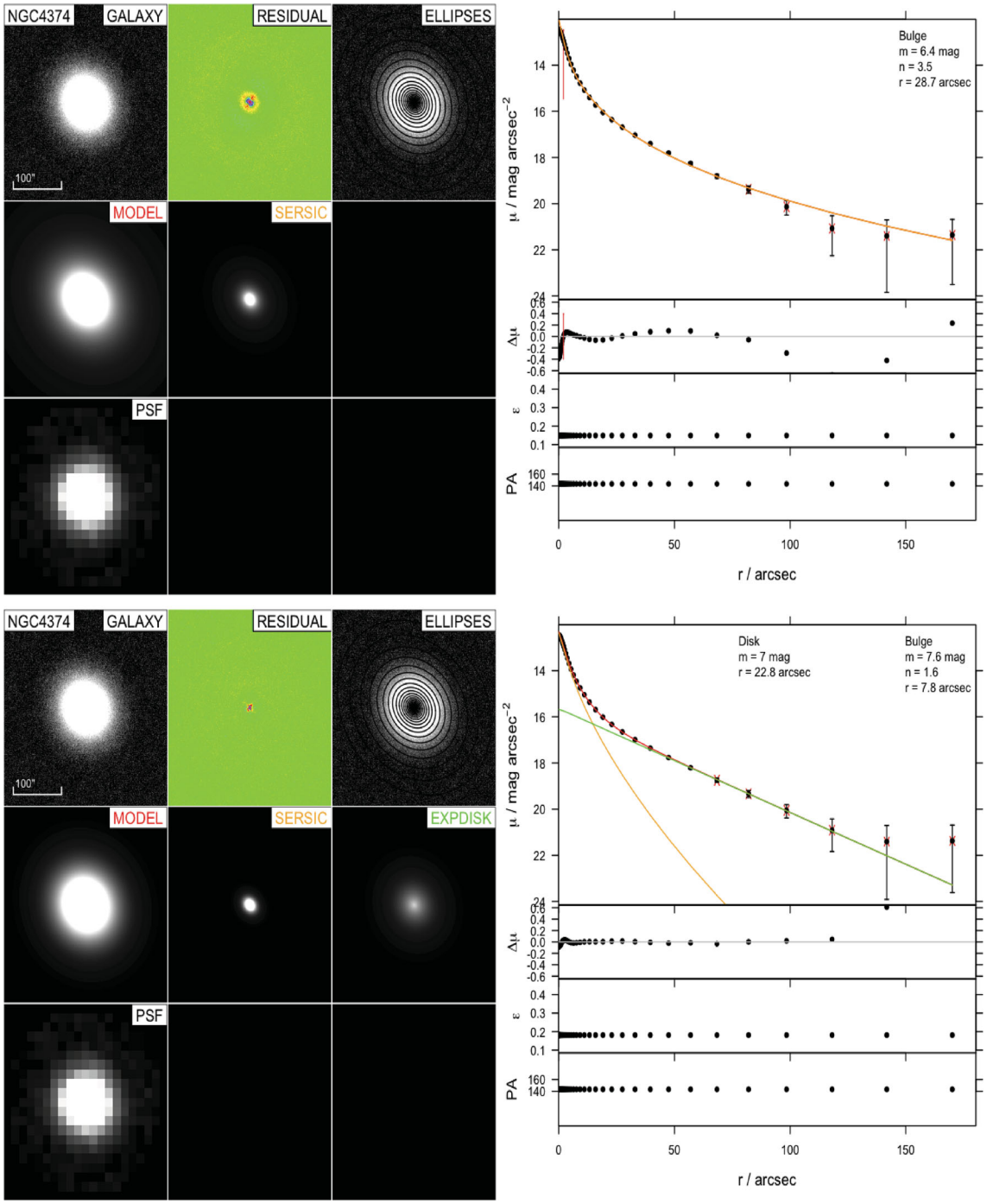

Figure 15. NGC 4374 has been classified as an high Sérsic index elliptical galaxy from previous studies. We believe that NGC 4374 can also be profiled with a two-component model. The layout is as in Fig. 5.

galaxy corresponds to the radio source (3C 270) which contains a pair of highly symmetric kpc-scale jets (Birkinshaw & Davies 1985) and an edge-on nuclear disc of gas and dust in the optical (Ferrarese, Ford & Jaffe 1996b; Jones et al. 2000; Ferrarese et al. 2006). In X-ray, it is possible that the galaxy hosts a heavily obscured AGN (Zezas et al. 2005). The isophotal analysis shows boxy isophotes at large radii both in the optical and near-IR bands (van den Bosch et al. 1994; Ferrarese, Ford & Jaffe 1996b; Quillen, Bower & Stritzinger 2000). GD07 derived a Sérsic index fit of $n = 7.3$.

NGC 4303 (M61) is a double-barred AGN galaxy (Erwin 2004) with bright star-forming regions in a ring around the nucleus and in the spiral arms in the ultraviolet (Colina et al. 1997) and also visible in near-IR images (Möllenhoff & Heidt 2001). Weinzirl et al. (2009) performed a 2D bulge–disc–bar decomposition using GALFIT3 on H-band images and derived $n = 1.55$, 1.0 and 0.55. Fisher & Drory (2010) showed that the spheroid component of the galaxy is a pseudo-bulge with $n_{\rm bulge} = 1.7$.

NGC 4342 is an S0 elongated galaxy with discy isophotes (van den Bosch et al. 1994). Bosch, Jaffe & van der Marel (1998)

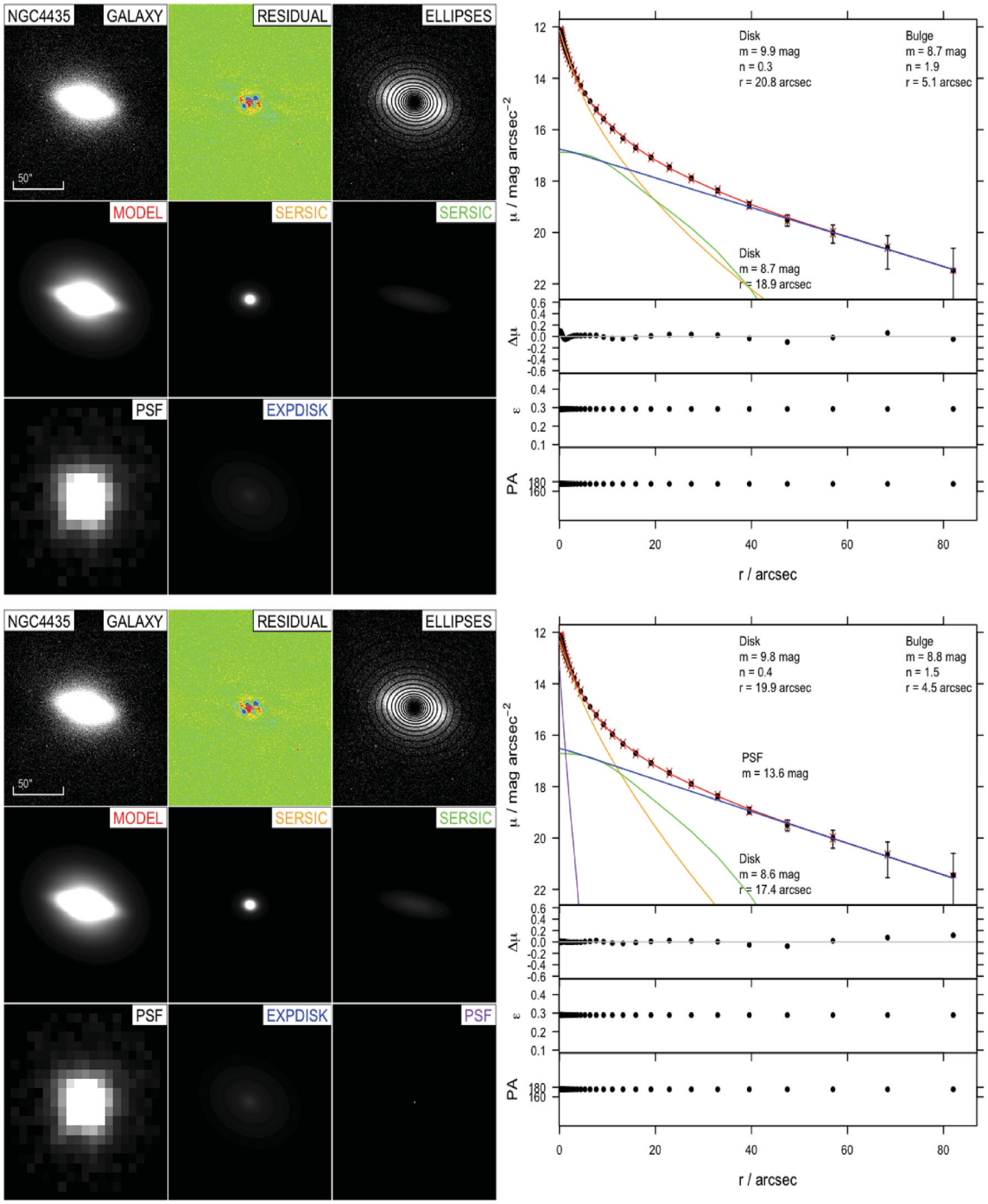

Figure 16. The surface brightness profile for NGC 4435 for different fits: (a) double Sérsic + exponential model and (b) double Sérsic + exponential model + PSF nuclei. The layout is as in Fig. 5.

discovered the existence of a nuclear disc in addition to the outer disc through analysis of the rotation curve in *Hubble Space Telescope* (*HST*)/WFPC2 *U*-, *V*- and *I*-band imaging.

NGC 4374 (M84, 3C 272.1) is a radio elliptical galaxy. GD07 found $n_{bulge} = 4.97$, while Kormendy et al. (2009, hereafter KF09) found $n_{bulge} = 7.9$ after excluding the inner 4.2 arcsec.[5]

NGC 4435 has boxy isophotes in the inner region and discy isophotes at large radii (Ferrarese et al. 2006).

NGC 4459 is a Virgo lenticular galaxy. H09 modelled NGC 4459 with two components (bulge/disc $n_{bulge} = 2.5$). KF09 classified NGC 4459 as an elliptical galaxy and estimated a Sérsic index of $n = 3.16$.

NGC 4473 is an elliptical galaxy with primarily discy isophotes (Bender, Doebereiner & Moellenhoff 1988; van den Bosch et al. 1994). Its unusual surface profile brightness has aroused plenty of interest (see e.g. Byun et al. 1996; Ferrarese et al. 2006;

[5] KF09 derive their major axis surface brightness profiles via fitting elliptical isophotes allowing a boxy/discy parameter to vary (MIDAS/ESO).

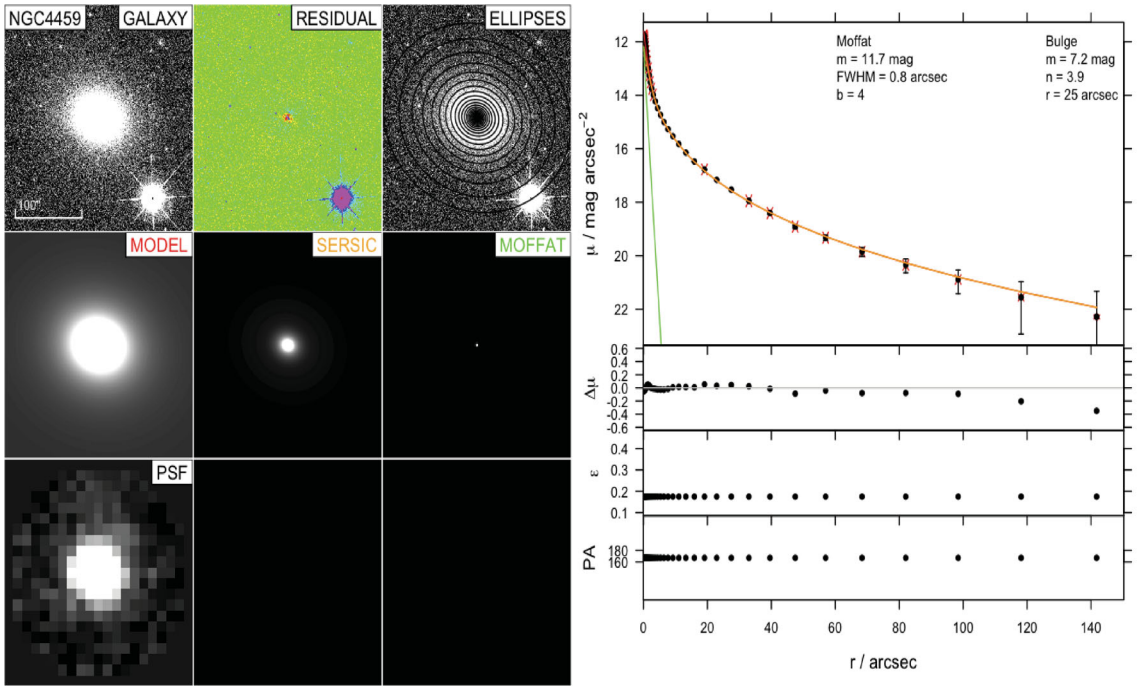

Figure 17. NGC 4459 has been classified as an S0 or as an elliptical galaxy from different studies. Our profiles show that is an elliptical galaxy with an extra light in the centre that needs to be masked or profiled. We found that the function that describes better this core light is the Moffat function. For more details about how we apply the Moffat function, see Section 3. The layout is as in Fig. 5.

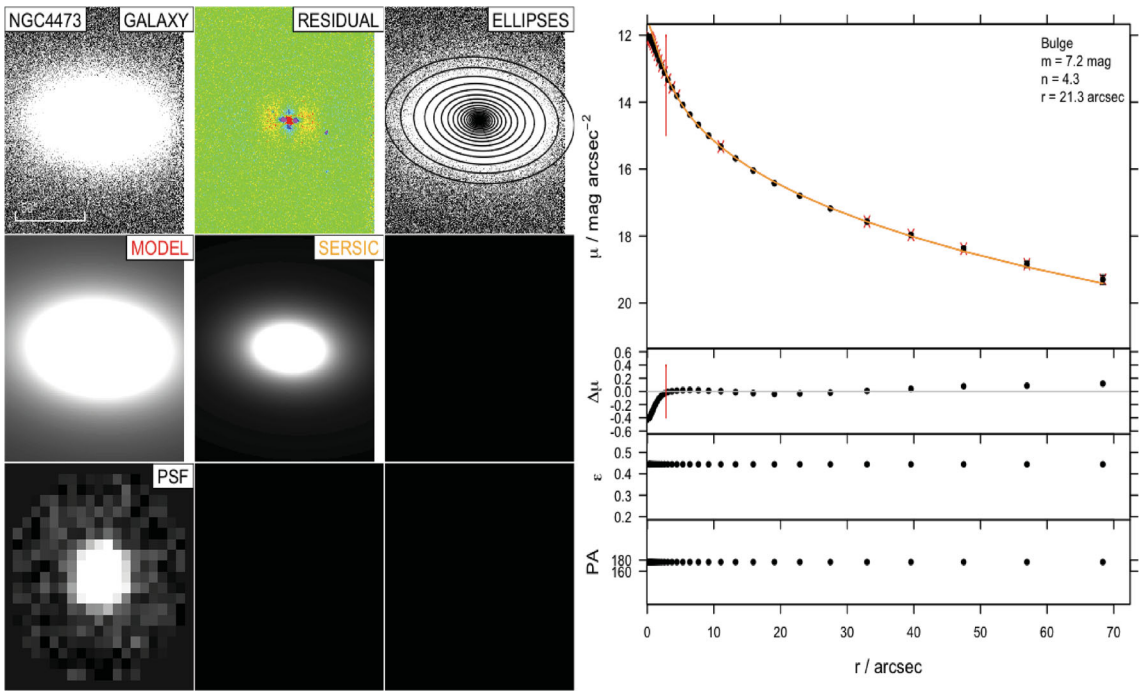

Figure 18. NGC 4473 has been classified as an elliptical galaxy with an inner rotating disc. We masked the inner 2.8 arcsec. The layout is as in Fig. 5.

Krajnović et al. 2006). The distribution of light in the inner part of the galaxy is dominated by a counter-rotating stellar disc (Cappellari et al. 2007). KF09 modelled the galaxy by excluding the inner 23 arcsec and measured a Sérsic index of $n = 4.0$ in agreement with the 2D profiling of H09. GD07 found a Sérsic index of $n = 2.73$.

NGC 4486 (M87) is the second brightest elliptical Virgo galaxy and classified as a cD due to extra halo light originating from the cluster. Ferrarese et al. (2006) and GD07 agreed on their Sérsic index measurements of 6.1 (using Sérsic-core model) and 6.8, respectively, while KF09 profiled with the extra halo and found $n = 11.86$. A big discrepancy in the Sérsic values appears when we transferred

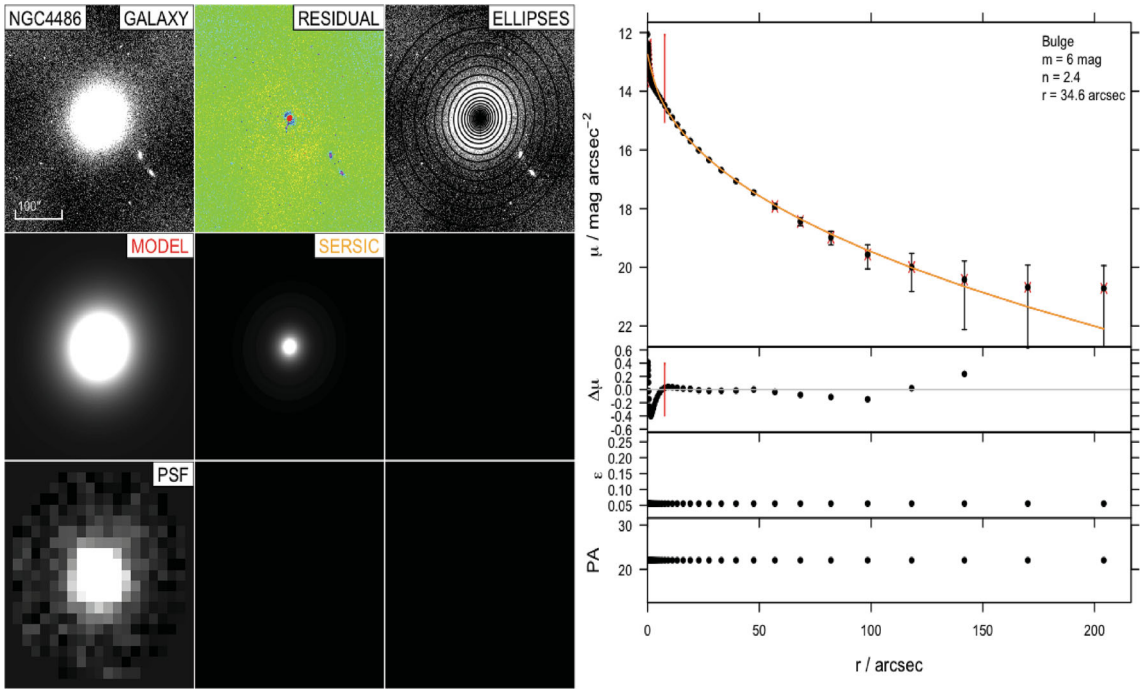

Figure 19. M87 is an elliptical galaxy with a recognizable jet in most of the wavelengths. We masked the inner 7.5 arcsec. Note the Sérsic index variance between 1D and 2D profiles (see Section 3.2). The layout is as in Fig. 5.

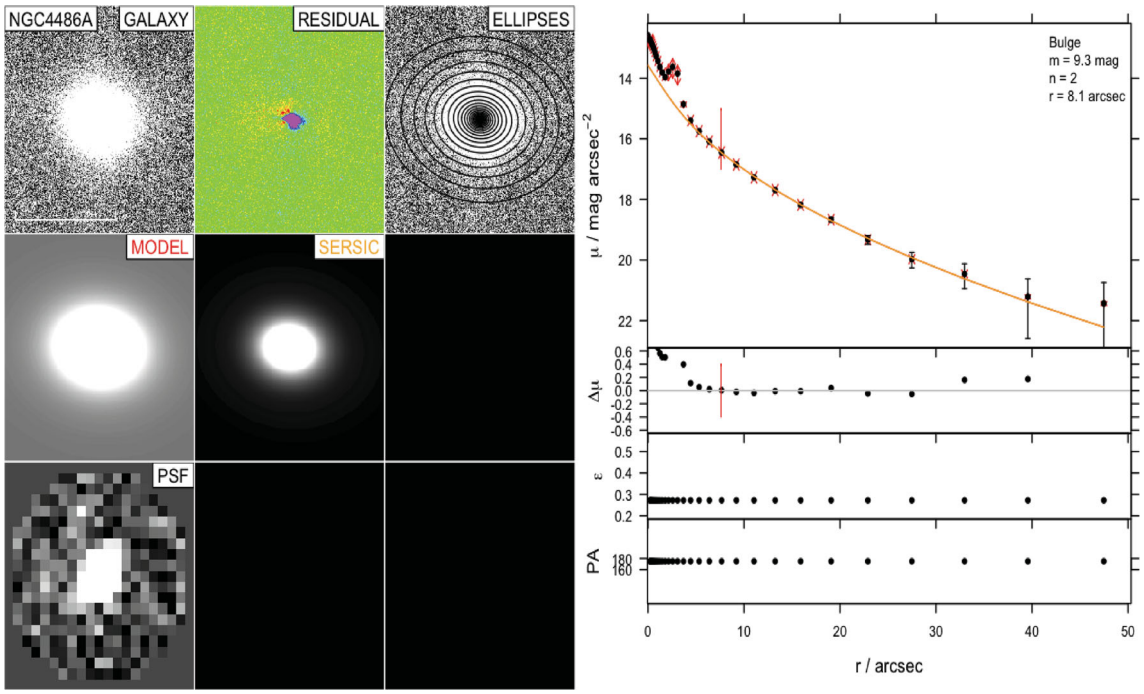

Figure 20. For profiling NGC 4486A, we masked the inner 7 arcsec where the flux is contaminated by a star placed next to the core of the galaxy. The layout is as in Fig. 5.

to 2D profiling where both D'Onofrio (2001) and H09 found a significantly low Sérsic index $n = 3.0$.

NGC 4486A has extra light from the nuclear disc visible in almost all wavelengths. In combination with a very bright star next to the centre, it is difficult to provide a reliable fit at the centre. Ferrarese et al. (2006), KF09 and H09 found Sérsic indices values 2.7, 2.04 and 4.2, respectively.

NGC 4486B is a low-luminosity dwarf galaxy with extra light near the centre and characterized by a double core (Lauer et al. 1996) which flattens the profile close to the nucleus. Due to its orbit around

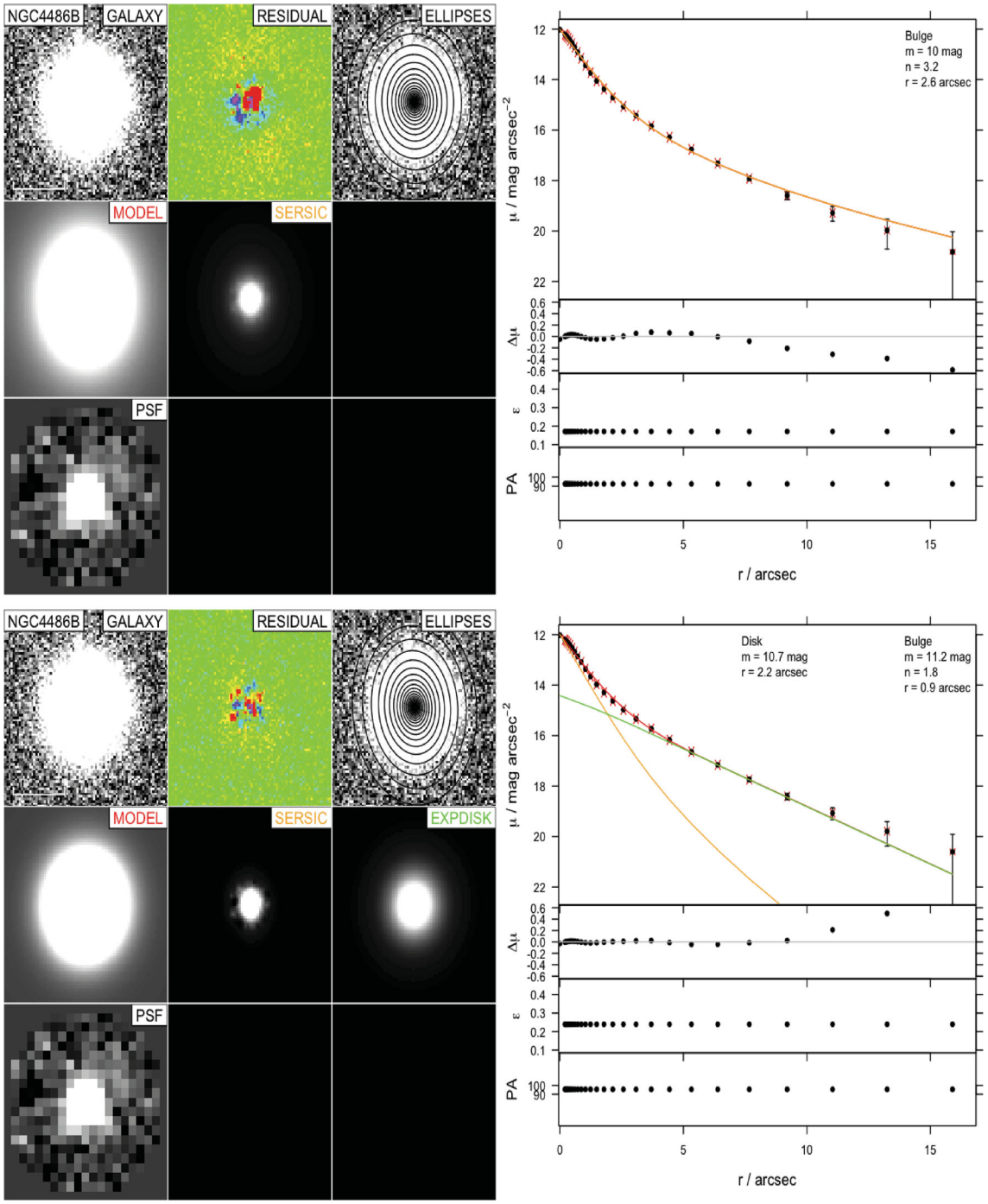

Figure 21. NGC 4486B has been characterized as a low-luminosity cE0 with extra light in the centre. Our surface brightness profile for NGC 4486B for two different fits: (a) single Sérsic and (b) Sérsic + exponential. The layout is as in Fig. 5.

NGC 4486, a fraction of the light from NGC 4486b is actually halo light from its companion and consequently affects the surface brightness of NGC 4486b. KF09 estimated a Sérsic index of $n = 2.2$ after modelling the additional light from NGC 4486 and masking the inner 1.3 arcsec. Soria et al. (2006) found $n = 2.7$.

NGC 4552 (M89) – Caon, Capaccioli & D'Onofrio (1993) first profiled this S0 galaxy with a single Sérsic index of $n = 13.87$ excluding the inner 2 arcsec, while KF09 applied the same model and found $n = 9.1$. Ferrarese et al. (2006) applied a core-Sérsic model and found $n_g = 7.1$. Finally, in 2D modelling, D'Onofrio (2001) and H09 used a bulge/disc model ($n_{bulge} = 4.2, 4.6$), yielding a much lower n value.

NGC 4564 has been classified as elliptical in RC3, while Trujillo et al. (2004) classified it as an S0 galaxy. The existence of the disc is also verified by GD07 and KF09 with a bulge Sérsic index value of 3.15 and 4.69, respectively. Also H09 found $n_{bulge} = 3.6$ plus an exponential disc.

NGC 4596 bar properties have been studied by Kent (1990) and Erwin (2005). H09 found $n_{bulge} = 3.3$, $n_{bar} = 1.0$ plus an exponential disc.

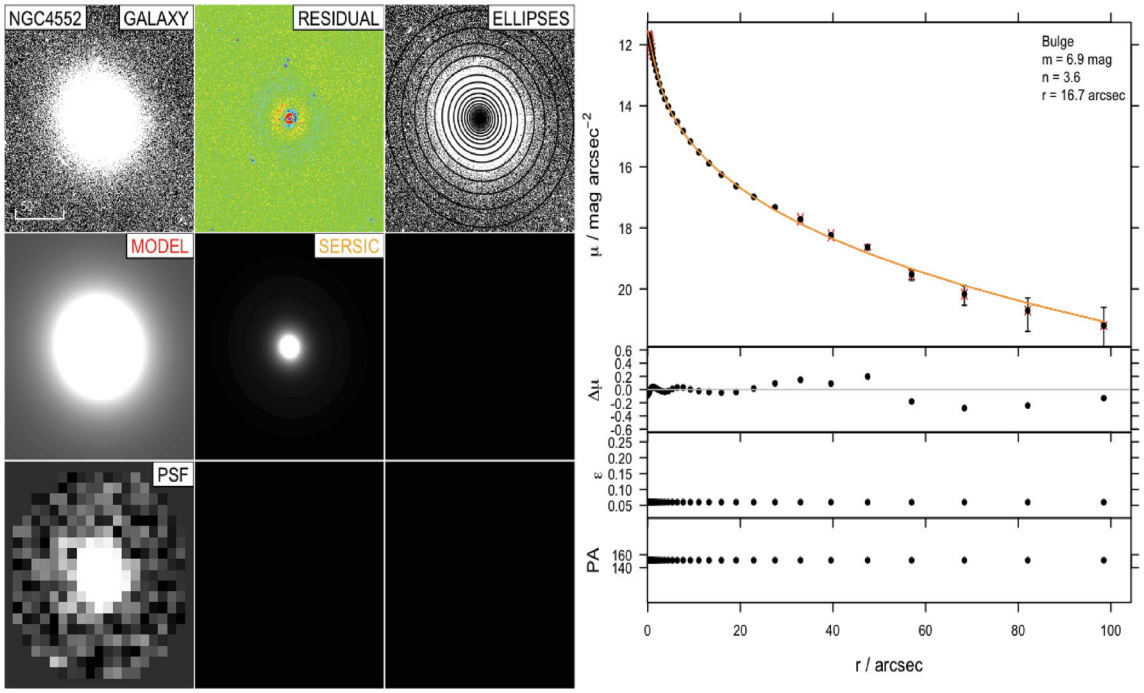

Figure 22. Note the Sérsic index variance between 1D and 2D profiles (see Section 3.2). The layout is as in Fig. 5.

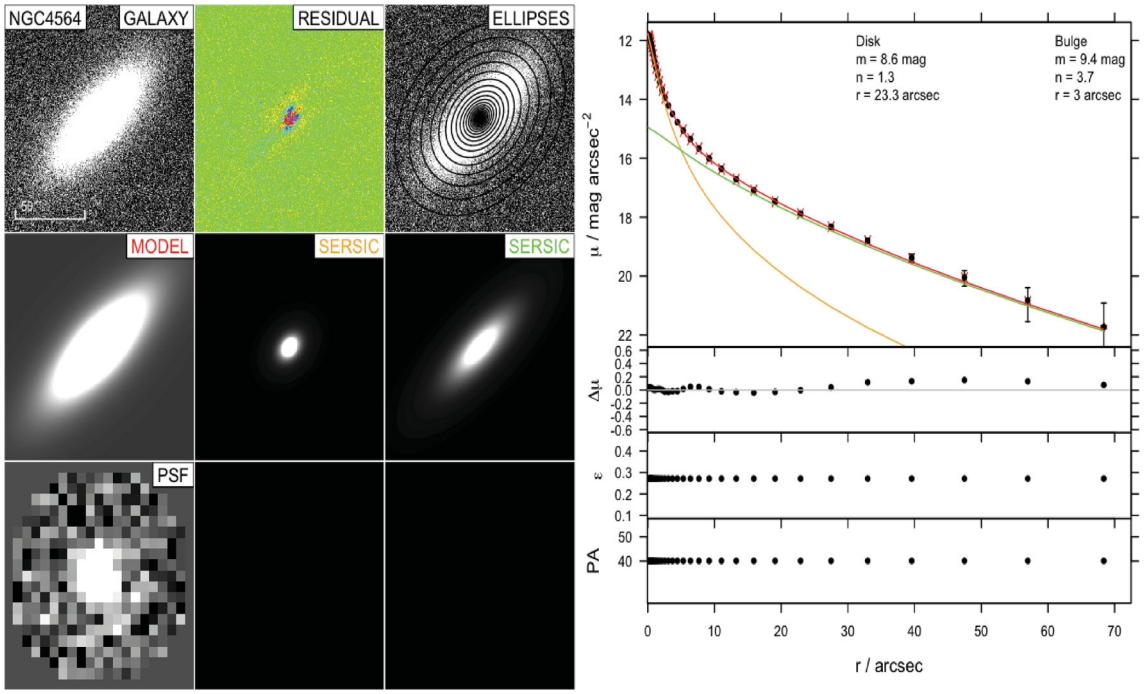

Figure 23. The NGC 4564 best fit is with a double Sérsic model. The layout is as in Fig. 5.

NGC 4621 (M59) – Ferrarese et al. (2006) and KF09 profiled NGC 4621 with a single Sérsic index and found $n_{bulge} = 6.8$ and 5.36, respectively, while H09 applied a bulge/disc model and found $n_{bulge} = 4.1$.

NGC 4649 – Ferrarese et al. (2006) found $n_{bulge} = 4.7$ plus core, while GD07 and H09 fitted single Sérsic model and derived $n_{bulge} = 6.04$ and 3.4, respectively.

NGC 4697 – GD07 measured $n = 4.0$, while H09 found $n_{bulge} = 3.0$ plus an exponential disc.

NGC 5576 is an elliptical galaxy which Trujillo et al. (2004) profiled with both a single Sérsic model ($n = 4.47$) and a Sérsic plus core model ($n = 4.89$).

NGC 5813 is an elliptical galaxy with a core (Lauer et al. 1995; Rest et al. 2001). H09 profiled with a bulge/disc model $n_{bulge} = 4.6$.

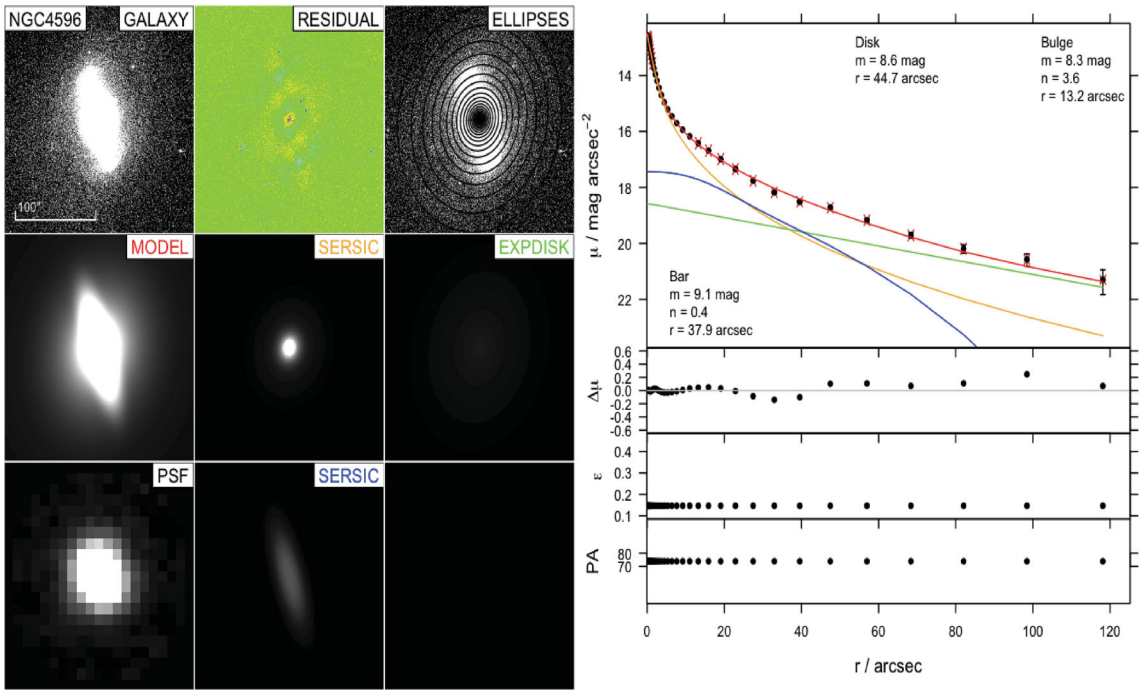

Figure 24. The surface brightness profile for NGC 4596. The layout is as in Fig. 5.

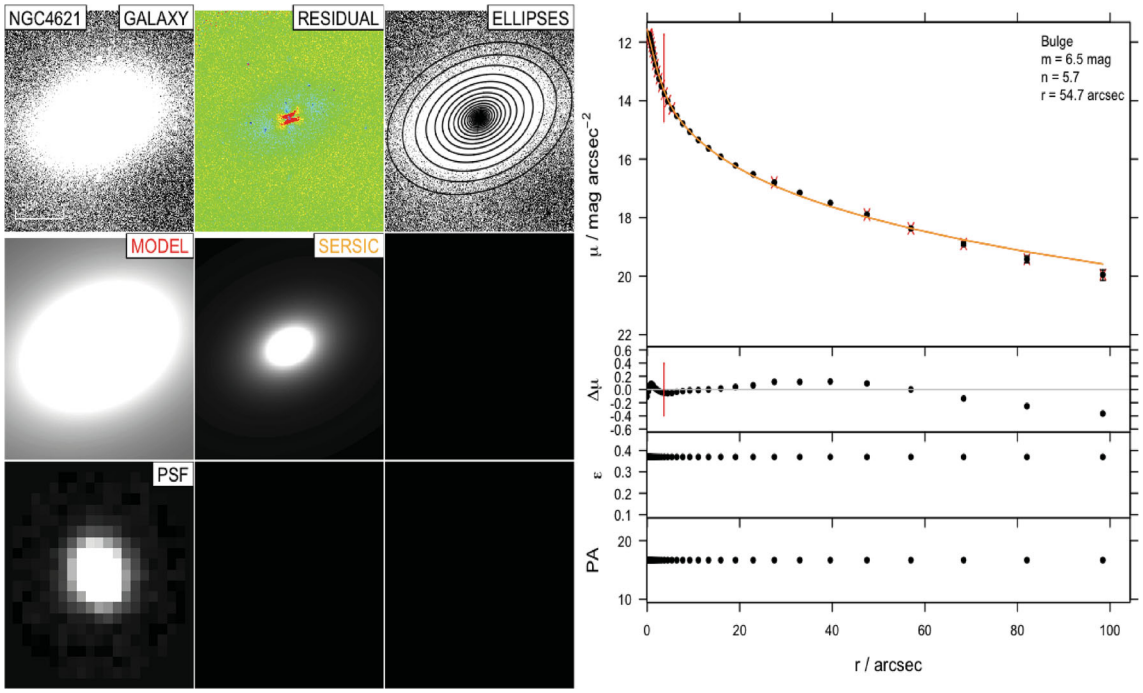

Figure 25. NGC 4621 has been classified as an S0 and as an elliptical galaxy from different studies. We do not find evidence of a disc, but the existence of a core which we masked (3.6 arcsec). The layout is as in Fig. 5.

NGC 5845 is a dwarf elliptical galaxy in the group of NGC 5846 with an unusually high central surface brightness. It hosts a nuclear disc and dust disc that extends to 15 arcsec on the major axis (Quillen et al. 2000; Mahdavi, Trentham & Tully 2005). GD07 and Trujillo et al. (2004) performed 1D profiling of the V-band images and derived a Sérsic index of $n = 3.22$ (single Sérsic fit) and $n = 2.88$ (Sérsic fit plus core fit), respectively. H09 found $n = 4.6$.

NGC 5846 is the main galaxy in an isolated group of 250 galaxies (Mahdavi et al. 2005) with a compact radio core at the optical centre (Moellenhoff, Hummel & Bender 1992). Forbes, Brodie & Huchra (1997) found slightly boxy isophotes in central regions,

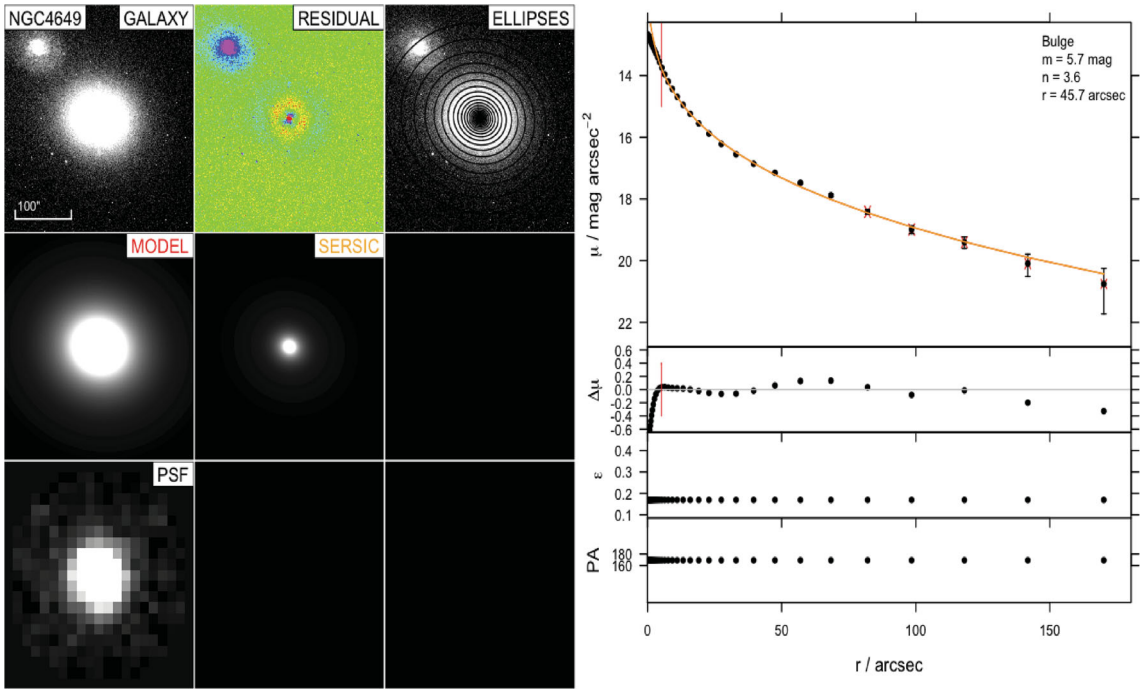

Figure 26. The surface brightness profile for NGC 4649; we masked the inner 5.2 arcsec. The layout is as in Fig. 5.

while Rest et al. (2001) argued that due to strong dust filaments it is not possible to study the nucleus and have reliable information about the isophotal shape. H09 modelled the galaxy light profile with a single Sérsic and found $n = 3.1$.

NGC 7052 is an isolated radio galaxy with an edge-on dust ring along the major axis (Nieto et al. 1990) and nuclear disc of gas/dust (de Juan, Colina & Golombek 1996) which affects the boxy/discy measurements of isophotes in the outer regions of the galaxy (Quillen et al. 2000). GD07 and H09 modelled the galaxy light profile and estimated Sérsic indices of $n = 4.55$ and =3.4, respectively.

UGC 9799 (3C 317) is the central elliptical galaxy (cD morphological class; cf. Seigar, Graham & Jerjen 2007) of the cooling flow cluster, Abell 2052. It features a central X-ray excess and is host to an AGN evident as a bright, steep-spectrum radio source (e.g. Zhao et al. 1993) with a compact optical counterpart (Castro-Rodríguez & Garzón 2003; Seigar et al. 2007). Seigar et al. (2007) and Donzelli et al. (2007) also identify a distinct outer halo to UGC 9799 (consistent with its classification as a cD morphological type) in Jacobus Kapteyn Telescope *R* band and *HST* NICMOS *H*-band (*F160W*) imaging, respectively. After masking the inner ∼1–2 arcsec (to exclude the central AGN) and modelling the outer halo with an exponential light distribution, these authors recovered Sérsic index fits of $n = 1.2$ and 2.3 to its major axis surface brightness profile, respectively.[6]

Our fits to all these galaxies are shown in Figs 5–33, and the results of our profiles are tabulated in Table 3. Where the number of components is ambiguous, we show the alternative profiles and tabulate its results in Table 4.

[6] Both Seigar et al. (2007) and Donzelli et al. (2007) derived their major axis surface brightness profiles via fitting of 'perfect' (i.e. non-boxy/discy) elliptical isophotes to their galaxy images using IRAF ELLIPSE.

4 RESULTS

4.1 Fitting methodology

In Fig. 34, we plot the black hole masses versus the absolute bulge/elliptical *K*-band magnitude of the host galaxies. The fitting algorithm used to estimate the linear M_{bh}–L relation and the log-linear M_{bh}–n relation is the regression analysis given in Tremaine et al. (2002):

$$\chi^2 = \sum_{i=1}^{N} \frac{(y_i - \alpha - \beta x_i)^2}{\delta y_i^2 + \beta^2 \delta x_i^2}, \quad (3)$$

where $x = \log n$ or $x = M_{K,\mathrm{sph}}$, $y = \log(M_{bh}/M_{\odot})$ and δy_i and $\delta \chi_i$ are the errors of the x and y measurements. Tremaine et al. (2002) inserted the intrinsic scatter ϵ_0 of the M_{bh}–L and M_{bh}–n correlations by replacing δy_i with $(\delta y_i^2 + \epsilon_0^2)^{1/2}$, where ϵ_0 is computed by repeating the fit until $\chi^2/(N-2) = 1$. The uncertainty on the ϵ_0 is estimated when $\chi^2/(N-2) = 1 \pm \sqrt{2/N}$.

Here we assume that the errors cited in the literature are 1σ uncertainties if not clearly stated. We now implement a Monte Carlo method to derive the errors. To do this, we randomly perturb each SMBH mass and the galaxy magnitude in each case assuming a normal error distribution. We repeat the fit 1001 times, each time applying equation (3), assuming that the uncertainty is zero, consequently δy and δx are zero.

The final values for the intercept α and the slope β are then derived from the median value of the 1001 individual sets of α and β values, while the δy and the δx are the standard deviations. We can see an illustration of the method in the bottom of the right-hand panel of Fig. 34. The 1001 red points show the measurement distribution for NGC 221 around the mean value. There are an equal number of points in each quadrant.

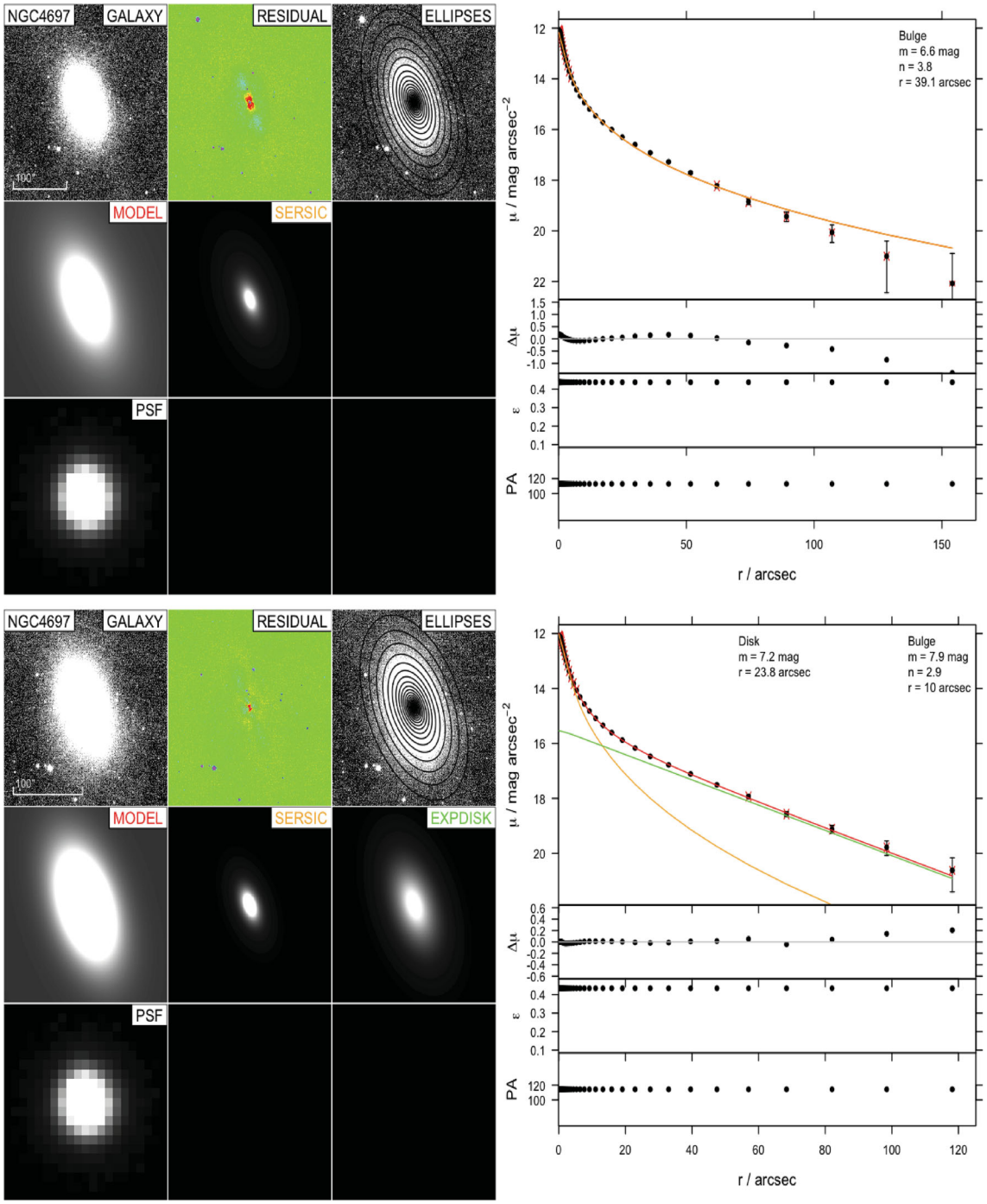

Figure 27. The surface brightness profile for NGC 4697. The layout is as in Fig. 5.

4.2 Robustness of mass measurements

A number of galaxies (NGC 863, 4435, 4486b and UGC 9799) have poorly constrained mass measurements. NGC 863 is the only galaxy in our sample for which the SMBH mass has been estimated via the method of reverberation mapping. Reverberation mapping masses use the local $M_{\rm bh}$–σ relation to normalize their values. Fig. 34 shows that NGC 863 is offset from the expected relation by $\sim$1 dex, while the virial mass estimation appears to be rather consistent with the $M_{\rm bh}$–L relation. NGC 4435 and UGC 9799 have only upper limit on their SMBH mass estimations. NGC 4486b SMBH mass measurement has been characterized as weak, while the mass estimation models show a possibility of zero mass black hole. For these reasons, the above referred galaxies have been excluded from the following fits.

4.3 $M_{\rm bh}$–L correlation

Fig. 34 shows the $M_{\rm bh}$–L distribution for our full sample with the error bars shown in the right-hand panel and various symbols indicating the morphological characteristics in the left-hand panel.

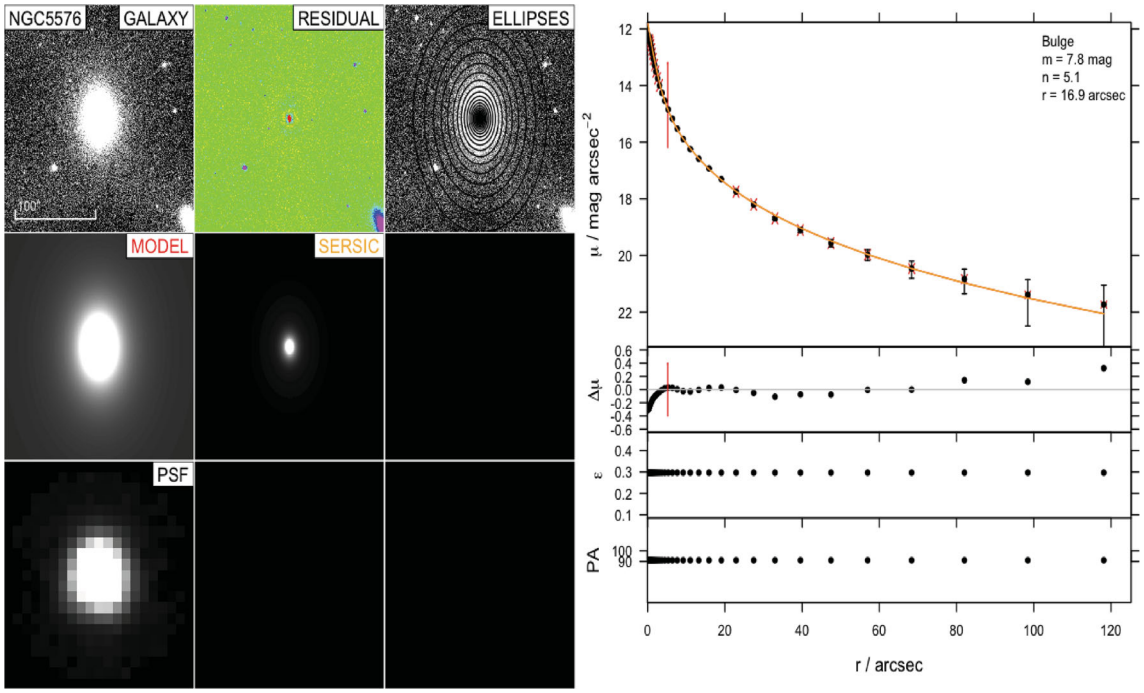

Figure 28. The surface brightness profile for NGC 5576; we masked the inner 5.2 arcsec. The layout is as in Fig. 5.

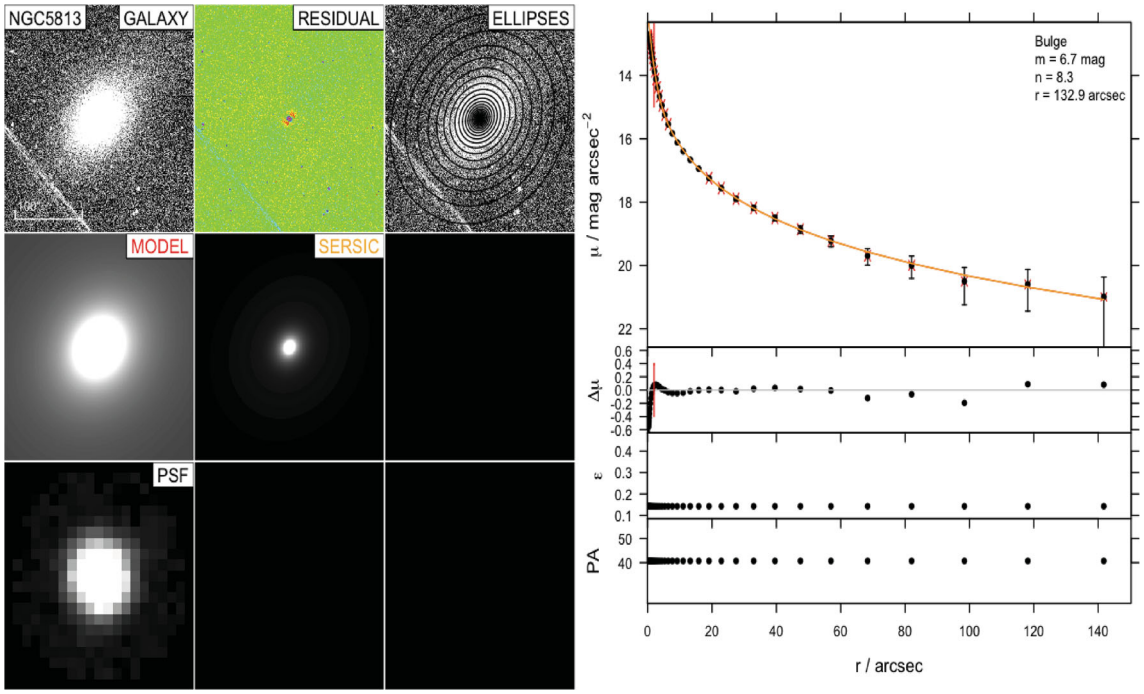

Figure 29. The surface brightness profile for NGC 5813; we masked the inner 2 arcsec. The layout is as in Fig. 5.

Applying equation (3) to our trustworthy sample of 25 galaxies, we derive

$$\log(M_{bh}/M_{\odot}) = -0.35(\pm0.024)(M_K + 18) + 6.2(\pm0.13), \quad (4)$$

with an intrinsic scatter of $0.52^{+0.1}_{-0.06}$ dex in $\log M_{bh}$. This level of intrinsic scatter is relatively high and may arise from the varied morphological mix of our sample (see Table 1).

If we exclude the barred galaxies (NGC 1068, 4258, 4303 and 4596), for which bulge fluxes are considered the most uncertain, and the extreme outlying galaxy NGC 4342 from the regression analysis, we derive

$$\log(M_{bh}/M_{\odot}) = -0.37(\pm0.03)(M_K + 18) + 6.1(\pm0.18), \quad (5)$$

with an intrinsic scatter of $0.43^{+0.09}_{-0.06}$ dex in $\log M_{bh}$ for a subsample of 20 galaxies.

Finally, if we additionally exclude the low-quality image cD galaxy, NGC 4486 (see Section 4.4), we find

$$\log(M_{bh}/M_{\odot}) = -0.36(\pm0.03)(M_K + 18) + 6.17(\pm0.16), \quad (6)$$

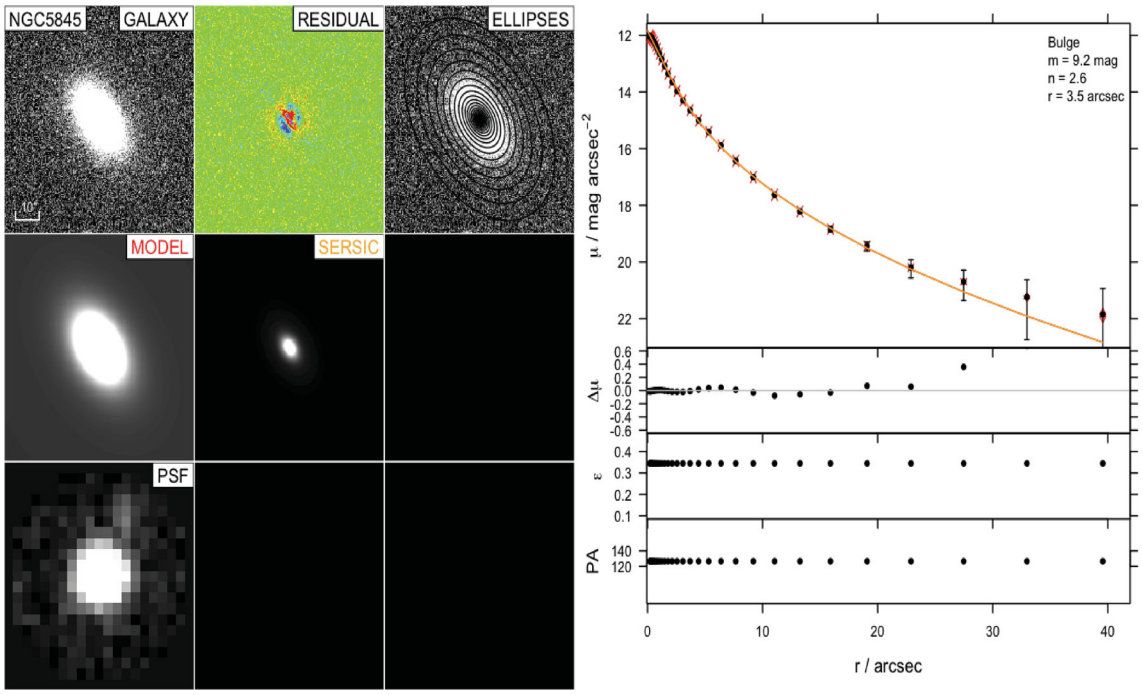

Figure 30. The surface brightness profile for NGC 5845. The layout is as in Fig. 5.

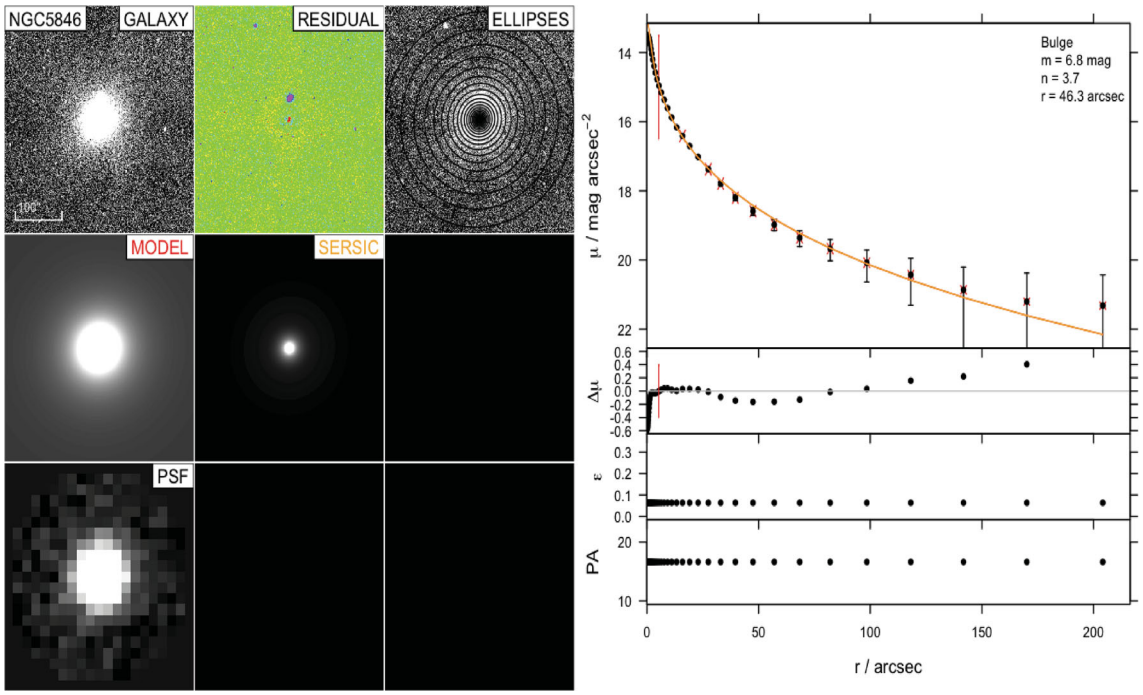

Figure 31. The surface brightness profile for NGC 5846; we masked the inner 5.2 arcsec. The layout is as in Fig. 5.

with an intrinsic scatter of $0.40^{+0.09}_{-0.06}$ dex in $\log M_{\rm bh}$ for a secure high-quality subsample of 19 galaxies.

When we apply the equation to our elliptical subsample consisting of 13 galaxies (again excluding NGC 4486), we obtain

$$\log(M_{\rm bh}/{\rm M}_{\odot}) = -0.42(\pm0.06)(M_K + 22) + 7.5(\pm0.15), \qquad (7)$$

with an intrinsic scatter of $0.31^{+0.087}_{-0.047}$ dex in $\log M_{\rm bh}$.

The red dotted line in Fig. 34 shows the Marconi & Hunt (2003) relation after Graham (2007) corrections have been applied. This relation has been derived from a sample of 26 galaxies (nine of which are within our sample) and has an intrinsic scatter of 0.35 dex [the best fit of Marconi & Hunt (2003) full sample, consisting of 37 galaxies gives an intrinsic scatter 0.51 dex]. From Fig. 34, we see that our $M_{\rm bh}$–L relation is found to be consistent with previous measurements. Previous near-IR $M_{\rm bh}$–L relations are based on 2MASS

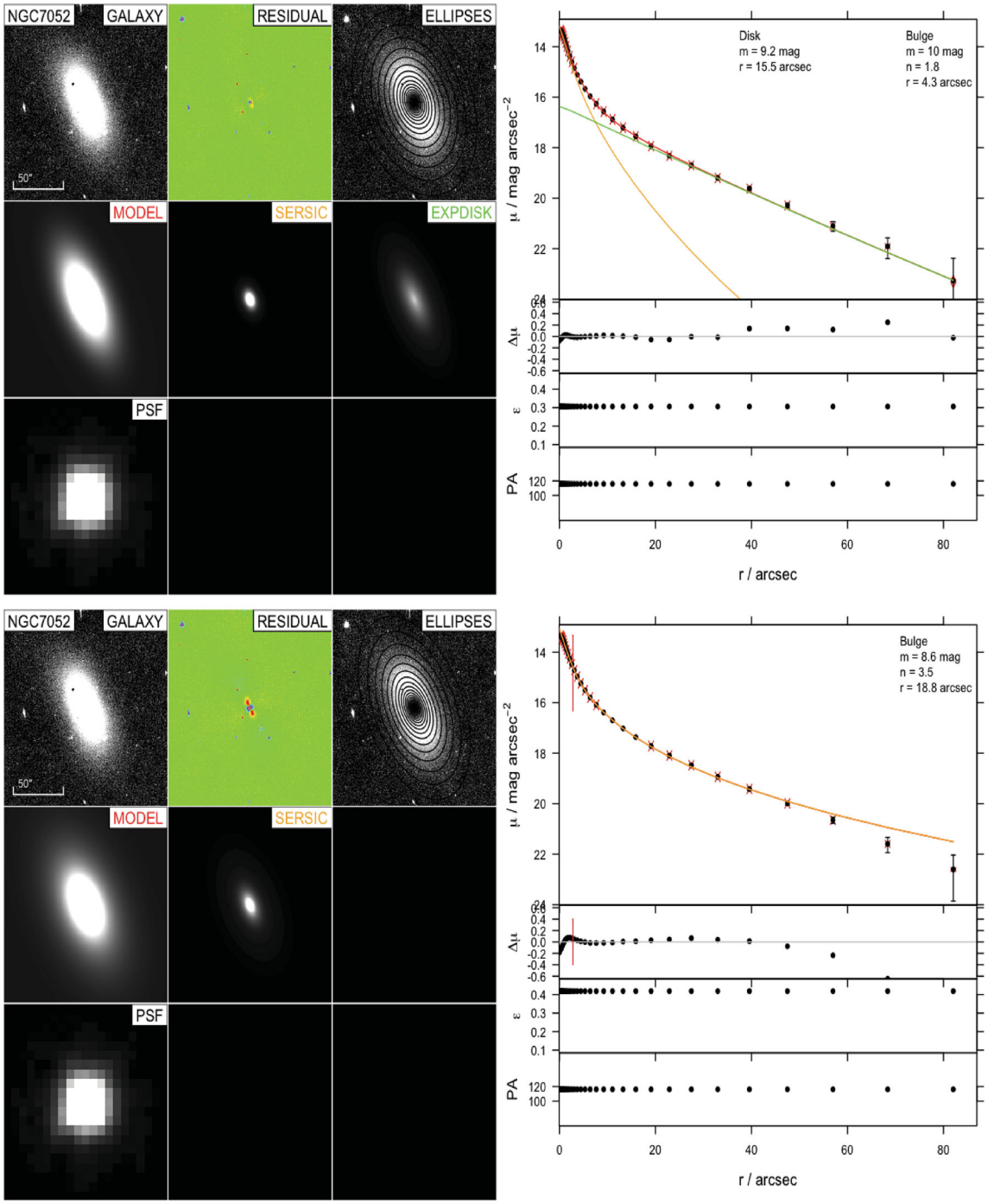

Figure 32. Previous studies model NGC 7052 with a single Sérsic model. We found that the galaxy can be profiled accurately by adding an additional component. The layout is as in Fig. 5.

data. The shallow nature of the 2MASS imaging makes it difficult to identify faint components of a galaxy. For instance, Marconi & Hunt (2003) misclassified NGC 221, 2778 and 4564 as elliptical galaxies.

We noted that the intrinsic scatter of the M_{bh}–L relation is increased when we include barred galaxies. The increased dispersion of the scatter could be the result of the uncertainty introduced by estimating the individual luminosity for each component. Also the barred galaxies in our sample have nuclei activity. Extracting the bulge luminosities for these galaxies is complex because of the contamination of the bulge flux from active nuclei.

In conclusion, we find that our high-quality data replicate but do not improve the intrinsic scatter, suggesting a genuine spread in the data $\epsilon_0 = \pm 0.31$. We note the significant uncertainty when including multiply component systems $\epsilon_0 = \pm 0.52$.

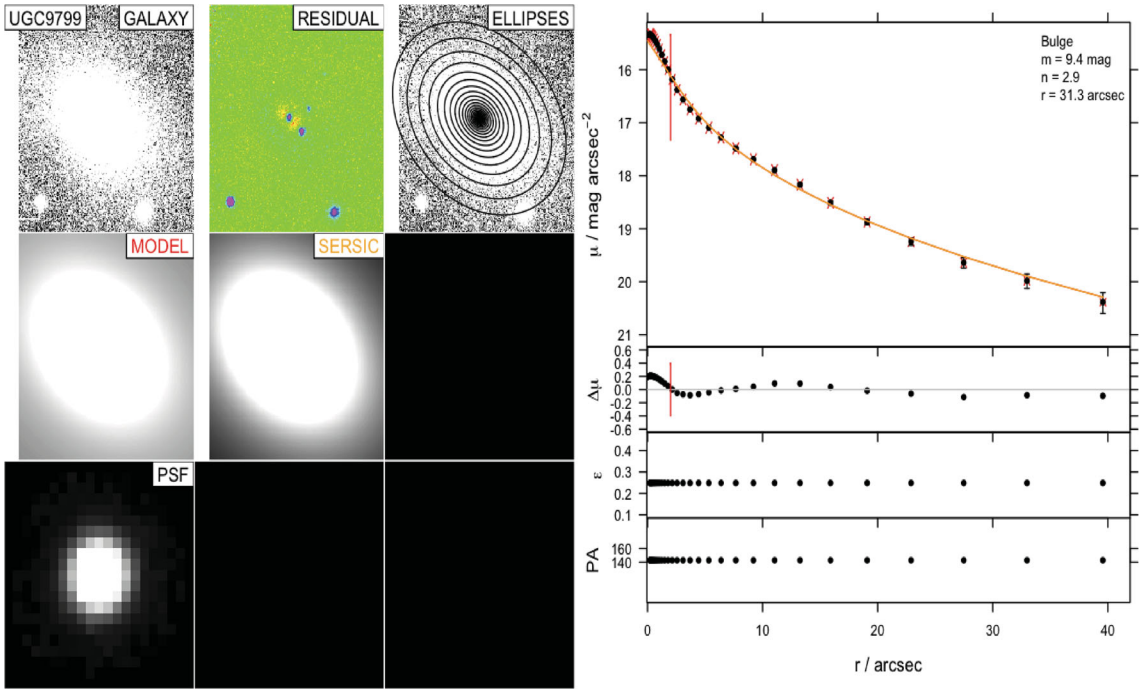

Figure 33. The surface brightness profile for UGC 9799; we masked the inner 2 arcsec. The galaxy is placed at the edge of the image that makes difficult to constrain the fit. The layout is as in Fig. 5.

4.4 M_{bh}–n correlation

Fig. 35 shows the M_{bh} as a function of Sérsic indices in the K band. The sample selection is the same as that noted is Section 4.3. Contrary to expectations, our Sérsic index values do not show strong correlation with M_{bh}.

In Fig. 36, we compare our Sérsic indices with Sérsic indices from the literature. In the left-hand panel of Fig. 36, we plot M_{bh} versus the Sérsic indices found in the literature for 16 galaxies matching our sample. These measurements are derived for R-, V-band images using 1D profiling (listed in Tables 6 and 7). The right-hand panel shows the M_{bh} versus this study's Sérsic indices. Individual comparisons for each galaxy's Sérsic index can be found in Section 3.2.

The tight relation between the M_{bh} and Sérsic index found in 1D optical analysis disappears in our 2D near-IR study. We note that 2D analysis appears to have an upper limit of $n \sim 5$. Especially, massive elliptical galaxies like NGC 4261, 4486 and 452 appear to have small Sérsic indices. In the case of NGC 4486, we suspect that the sky gradient of the image obstruct us from fitting the halo of the galaxy. The discrepancy between the different studies therefore appears to be a result of either the method used to model the galaxy (i.e. 1D versus 2D) and/or the transfer from optical wavelength to K-band images.

Kelvin et al. (in preparation) perform multiwavelength 2D profiling in nine bands, from u to K band, with GALFIT3, finding no important change of Sérsic indices for early-type systems in moving from r band to near-IR. However, discs and disc components are noted to show an increase in Sérsic index with wavelength and lowering in half-light radii. It appears then that the distinction between disc and bulge is less pronounced in the near-IR data compared to the optical.

We believe that a further cause of the mismatch could be the different pixel weighting adopted by 1D versus 2D studies. GALFIT3 weights pixels using a σ (weight) map. The σ map shows the one standard deviation of counts at each pixel. Such maps can be created by the program itself or supplied by the user. We chose to follow GALFIT3 manual suggestion and let the program create the maps internally (see Appendix A for details). The only input values required for the σ images to be produced internally are the background sky value and the rms scatter of the background sky value.

Another known source of uncertainty of the Sérsic index is the switch from major axis fitting to minor axis fitting (Caon et al. 1993). Ferrari et al. (2004) showed that major axis and minor axis Sérsic index mismatch occurs when there are radial variations of the isophotal eccentricity.

Further work is required to investigate what causes the breakdown of the M_{bh}–n correlation. Vika et al. (in preparation) will pursue this by exploring the photometric properties derived from 1D and 2D fits for a larger sample of ∼200 elliptical galaxies and the contribution of different pixel weights.

Our conclusion is that the M_{bh}–n relation is no longer clearly apparent in the high-quality near-IR data. We believe that this is caused by a combination of the use of 2D fitting in conjunction with the difficulty to distinguish the bulge and disc components in near-IR data. While we cannot rule out minor errors in the profiling process, we have explored a variety of alternative fits with extensive masking. As the motivation was to derive an M_{bh}–n relation suitable for application to automated GALFIT3 analysis, we must conclude that the M_{bh}–n relation is unsuitable for such use either because of a breakdown of the relation when 2D fitting is used or the excessive care required to mitigate the core deviations.

5 SUMMARY

One of the main motivations of this study was to derive M_{bh}–L and M_{bh}–n relations using high-quality near-IR data and using the same methods that we will apply to the GAMA survey in order to derive the SMBH mass function (e.g. Vika et al. 2009). In this paper, we

Table 6. Galaxy sample. Column (2): the distances have come from Tonry et al. (2001) unless otherwise specified. Column (3): the black hole masses have been adjusted to the distance given in column (2). Column (4): the method of measuring the black hole mass: s – stellar kinematics, g – gas kinematics, m – water masers, p – stellar proper motion and r – reverberation mapping. Columns (5–6): Sérsic indices and their band. References: (1) Verolme et al. 2002; (2) Peterson et al. 2004; (3) Lodato & Bertin 2003; (4) Gebhardt et al. 2003; (5) Henkel et al. 2002; (6) Barth et al. 2001; (7) Herrnstein et al. 1999; (8) Shen & Gebhardt 2010; (9) Siopis et al. 2009; (10) Ferrarese et al. 1996b; (11) Pastorini et al. 2007; (12) Jerjen, Binggeli & Barazza 2004; (13) Cretton & van den Bosch 1999; (14) Maciejewski & Binney 2001; (15) Coccato et al. 2006; (16) Sarzi et al. 2001; (17) Macchetto et al. 1997; (18) Ferrarese et al. 1996a; (19) Nowak et al. 2007; (20) Valluri, Merritt & Emsellem 2004; (21) Kormendy et al. 1997; (22) Cappellari et al. 2008; (23) Dalla Bontà et al. 2009; (24) NED/Virgo + GA + Shapley corrected Hubble flow distances; (25) van der Marel & van den Bosch 1998; (26) GD07; (27) KF09; (28) Seigar et al. 2007; (29) Gültekin et al. 2009a; (30) Gebhardt & Thomas 2009.

Galaxy name (1)	Distance (Mpc) (2)	M_{bh} (10^8 $M_\odot$) (3)	Method (ref) (4)	n_{sph} (mag) (5)	Band (ref) (6)
NGC 221	0.86	$0.025^{+0.005}_{-0.005}$	s (1)	1.32	*R* (26)
NGC 863	7.4 (24)	$0.47^{+0.074}_{-0.074}$	r (2)	–	–
NGC 1068	15.2 (24)	$0.084^{+0.003}_{-0.003}$	m (3)	–	–
NGC 2778	22.3	$0.15^{+0.09}_{-0.10}$	s (4)	1.60	*R* (26)
NGC 2960	72.8 (24)	$0.12^{+0.03}_{-0.03}$	m (5)	–	–
NGC 3245	20.9	$2.1^{+0.5}_{-0.5}$	g (6)	–	–
NGC 4258	7.2 (7)	$0.3^{+0.2}_{-0.2}$	s (9)	2.04	*R* (26)
NGC 4261	31.6	$5.2^{+1.0}_{-1.1}$	g (10)	7.30	*R* (26)
NGC 4303	16.1 (18)	0.006-0.16	g (11)	–	–
NGC 4342	17.0 (12)	$3.3^{+1.9}_{-1.1}$	s (13, 20)	–	–
NGC 4374	18.4	$4.64^{+3.46}_{-1.83}$	g (14)	5.60	*V* (27)
NGC 4435	14.0 (24)	<0.075	g (15)	–	–
NGC 4459	16.1	$0.70^{+0.13}_{-0.13}$	g (16)	3.17	*V* (27)
NGC 4473	15.3	$1.2^{+0.4}_{-0.9}$	s (4)	2.73	*R* (26)
NGC 4486	16.1	34^{+10}_{-10}	g (17)	11.84	*V* (27)
NGC 4486a	17.0 (12)	$0.13^{+0.08}_{-0.08}$	s (19)	2.04	*V* (27)
NGC 4486b	17.0 (12)	$6.0^{+3.0}_{-2.}$	s (21)	2.2	*V* (27)
NGC 4552	15.3	$4.8^{+0.8}_{-0.8}$	s (22)	9.22	*V* (27)
NGC 4564	14.6	$0.60^{+0.03}_{-0.09}$	s (4)	3.15	*R* (26)
NGC 4596	17.0 (18)	$0.79^{+0.38}_{-0.33}$	g (16)	–	–
NGC 4621	18.3	$4.0^{+0.6}_{-0.6}$	s (22)	5.36	*V* (27)
NGC 4649	16.8	$22.0^{+4.0}_{-6.0}$	s (4)	6.04	*R* (26)
NGC 4697	11.4	$1.8^{+0.2}_{-0.1}$	s (4)	4.00	*R* (26)
NGC 5576	24.8	$1.8^{+0.3}_{-0.4}$	s (29)	–	–
NGC 5813	32.2	$7.0^{+1.1}_{-1.1}$	s (22)	–	–
NGC 5845	25.2	$2.6^{+0.4}_{-1.5}$	s (4)	3.22	*R* (26)
NGC 5846	24.9	$11.0^{+2.0}_{-2.0}$	s (22)	–	–
NGC 7052	66.4 (24)	$3.7^{+2.6}_{-1.5}$	g (25)	4.55	*R* (26)
UGC 9799	141 (23)	<46.0	g (23)	1.4	*R* (28)

tested the M_{bh}–L and M_{bh}–n relations using updated SMBH masses and provide new estimations of the galaxy component luminosities and light profile shapes. We made use of *K*-band galaxy images for a sample of 29 galaxies taken by WFCAM as part of the UKIDSS-LAS.

We used GALFIT3 to produce 2D surface brightness photometry on *K*-band images and decomposed the different components of the host galaxy. We carefully modelled all the components of each galaxy and derived estimates of the various structural parameters for each galaxy along with a concise discussion of each galaxy's previous studies at optical wavelengths.

Table 7. Galaxy sample. Additional SMBH mass–galaxy distance measurements. The layout is as in Table 6.

Galaxy name (1)	Distance (Mpc) (2)	M_{bh} (10^8 $M_\odot$) (3)	method (ref) (4)
NGC 4486	17.9	64^{+5}_{-5}	s (30)
NGC 4649	15.7	45^{+10}_{-10}	s (8)

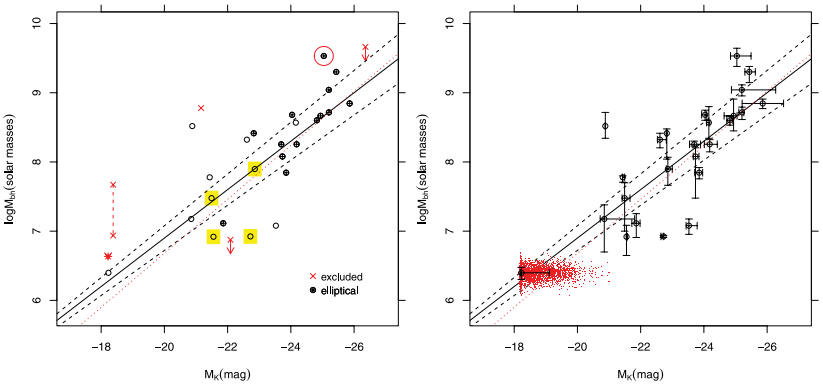

Figure 34. Left-hand panel: the $M_{\rm bh}$–L_K relation for the full sample (solid line) with 1σ uncertainty (dashed line). The circles with a cross indicate elliptical galaxies. The yellow rectangular symbol denotes galaxies with bar. The red dotted line comes from Graham et al. (2007, equation13). The four galaxies excluded for the fitting (red crosses) are NGC 863, 4435, UGC9799 and NGC 4486B. The red star indicates the position of the Milky Way which has not been included in the line fit but shown merely for reference. The red dashed line connects the two possible black hole masses for the galaxy NGC 863. The red circle indicates the galaxy NGC 4486. Right-hand panel: same plot as the left-hand panel, with the addition of the individual error bars. See Section 4.3 for details.

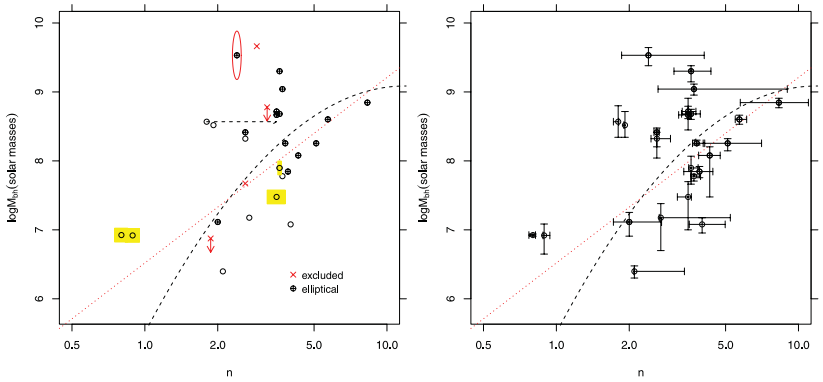

Figure 35. The SMBH mass versus the spheroid Sérsic index in the K-band. Different groups of galaxies are indicated with different symbols as in Fig. 34. The black dashed line indicates the Sérsic index of NGC 7052 for a single Sérsic fit. The linear and quadratic $M_{\rm bh}$–n relation of GD07 are shown as a red dotted line and a black dashed curve.

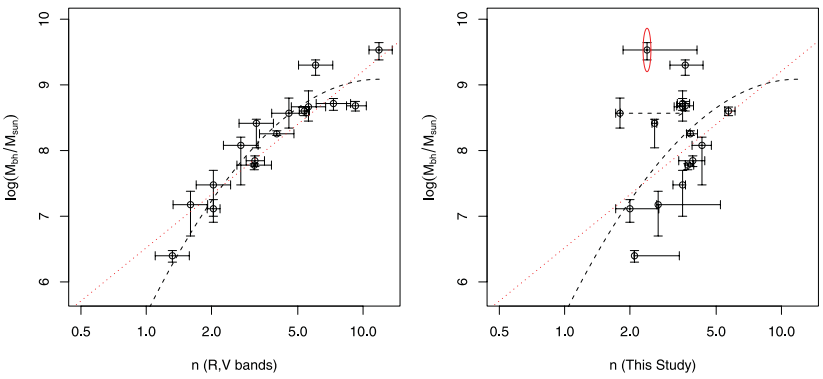

Figure 36. Comparison between this study's Sérsic index and values from literature. Left-hand panel: correlations between SMBH mass and the Sérsic index of the spheroid for a subset of our sample reported from 1D fitting in R and V bands by Graham & Driver (2007), KF09 and Seigar et al. (2007). Dotted and dashed lines are GD07 best linear and quadratic fits. Right-hand panel: the same galaxies as in left-hand panel but with the Sérsic indices derived from this study with 2D fit.

We have used 21 elliptical and disc systems with classical bulge galaxies to derive the $M_{\rm bh}$–L relation with intrinsic scatter of 0.41. We confirm a strong correlation between the central $M_{\rm bh}$ and its host galaxy's spheroid luminosity found from a number of previous studies. Overall, we see that the scatter of the $M_{\rm bh}$–L relation is much larger when we include bar galaxies and galaxies with active nuclei. We found no improvement of the intrinsic scatter for the $M_{\rm bh}$–L relation by using higher quality data which may indicate that we have reached the physical limit to which we can constrain the $M_{\rm bh}$–L relation.

Using the same sample of galaxies, we failed to find a clear $M_{\rm bh}$–n correlation, but we noted that the Sérsic index can vary significantly from study to study. The available data are inadequate for deriving accurate outcomes for the different Sérsic index values. Our best explanation is that the mismatch arises from the different weighting of pixel during the fit that each study uses. Further comparison of

1D analysis versus 2D analysis is required to fully understand this result.

In conclusion, we have established an M_{bh}–L relation based on GALFIT3 2D profiling of near-IR data which we will shortly apply to the GAMA data set (Vika et al., in preparation).

ACKNOWLEDGMENTS

This work is based in part on data obtained as part of the UKIRT Infrared Deep Sky Survey. The UKIDSS project is defined in Lawrence et al. (2007). UKIDSS uses the UKIRT Wide Field Camera (WFCAM; Casali et al. 2007) and a photometric system described in Hewett et al. (2006). The pipeline processing and science archive are described in Irwin et al. (2010, in preparation) and Hambly et al. (2008). We thank the referee for helpful suggestions that improve this paper.

REFERENCES

Alexander D. M. et al., 2008, AJ, 135, 1968
Alonso-Herrero A., Simpson C., Ward M. J., Wilson A. S., 1998, ApJ, 495, 196
Barth A. J., Sarzi M., Rix H., Ho L. C., Filippenko A. V., Sargent W. L. W., 2001, ApJ, 555, 685
Bender R., Doebereiner S., Moellenhoff C., 1988, A&AS, 74, 385
Bennert V. N., Treu T., Woo J., Malkan M. A., Le Bris A., Auger M. W., Gallagher S., Blandford R. D., 2010, ApJ, 708, 1507
Bertin E., Arnouts S., 1996, A&AS, 117, 393
Bettoni D., Falomo R., Fasano G., Govoni F., 2003, A&A, 399, 869
Birkinshaw M., Davies R. L., 1985, ApJ, 291, 32
Bock J. J. et al., 2000, AJ, 120, 2904
Borys C., Smail I., Chapman S. C., Blain A. W., Alexander D. M., Ivison R. J., 2005, ApJ, 635, 853
Bosch F. C., Jaffe W., van der Marel R. P., 1998, MNRAS, 293, 343
Byun Y. I. et al., 1996, AJ, 111, 1889
Caon N., Capaccioli M., D'Onofrio M., 1993, MNRAS, 265, 1013
Cappellari M. et al., 2007, MNRAS, 379, 418
Cappellari M. et al., 2008, in Bureau M., Athanassoula E., Barbuy B., eds, Proc. IAU Symp. 245, Formation and Evolution of Galaxy Bulges. Cambridge Univ. Press, Cambridge, p. 215
Casali M., Adamson A., Alves de Oliveira C., Almaini O., Burch K., Chuter T., Elliot J., 2007, A&A, 467, 777
Castro-Rodríguez N., Garzón F., 2003, A&A, 411, 55
Choi P. I., Guhathakurta P., Johnston K. V., 2002, AJ, 124, 310
Claussen M. J., Heiligman G. M., Lo K. Y., 1984, Nat, 310, 298
Coccato L., Sarzi M., Pizzella A., Corsini E. M., Dalla Bontà E., Bertola F., 2006, MNRAS, 366, 1050
Colina L., Garcia Vargas M. L., Mas-Hesse J. M., Alberdi A., Krabbe A., 1997, ApJ, 484, L41
Cretton N., van den Bosch F. C., 1999, ApJ, 514, 704
Dalla Bontà E., Ferrarese L., Corsini E. M., Miralda Escudé J., Coccato L., Sarzi M., Pizzella A., Beifiori A., 2009, ApJ, 690, 537
de Juan L., Colina L., Golombek D., 1996, AAP, 305, 776
D'Onofrio M., 2001, MNRAS, 326, 1517
Donzelli C. J., Chiaberge M., Macchetto F. D., Madrid J. P., Capetti A., Marchesini D., 2007, ApJ, 667, 780
Driver S. P., Liske J., Cross N. J. G., De Propris R., Allen P. D., 2005, MNRAS, 360, 81
Driver S. P., Popescu C. C., Tuffs R. J., Graham A. W., Liske J., Baldry I., 2008, ApJ, 678, L101
Driver S. P. et al., 2009, Astron. Geophys., 50, 050000
Drory N., Fisher D. B., 2007, ApJ, 664, 640
Dwek E. et al., 1995, ApJ, 445, 716
Erwin P., 2004, A&A, 415, 941
Erwin P., 2005, MNRAS, 364, 283
Ferrarese L. et al., 1996a, ApJ, 464, 568
Ferrarese L., Ford H. C., Jaffe W., 1996b, ApJ, 470, 444
Ferrarese L. et al., 2006, ApJS, 164, 334
Ferrari F., Dottori H., Caon N., Nobrega A., Pavani D. B., 2004, MNRAS, 347, 824
Fisher D. B., Drory N., 2010, ApJ, 716, 942
Forbes D. A., Brodie J. P., Huchra J., 1997, AJ, 113, 887
Gallimore J. F., Baum S. A., O'Dea C. P., Pedlar A., 1996, ApJ, 458, 136
Gaskell C. M., Kormendy J., 2009, in Jogee S., Marinova I., Hao L., Blanc G. A., eds, ASP Conf. Ser. Vol. 419, Galaxy Evolution: Emerging Insights and Future Challenges. Astron. Soc. Pac., San Francisco, p. 388
Gebhardt K., Thomas J., 2009, ApJ, 700, 1690
Gebhardt K. et al., 2003, ApJ, 583, 92
Gillessen S., Eisenhauer F., Fritz T. K., Bartko H., Dodds-Eden K., Pfuhl O., Ott T., Genzel R., 2009, ApJ, 707, L114
Glass L. et al., 2011, ApJ, 726, 31
Graham A. W., 2002, ApJ, 568, L13
Graham A. W., 2007, MNRAS, 379, 711
Graham A. W., 2008, Publ. Astron. Soc. Australia, 25, 167
Graham A. W., Driver S. P., 2005, Publ. Astron. Soc. Australia, 22, 118
Graham A. W., Driver S. P., 2007, ApJ, 655, 77 (GD07)
Graham A. W., Erwin P., Caon N., Trujillo I., 2001, ApJ, 563, L11
Graham A. W., Driver S. P., Allen P. D., Liske J., 2007, MNRAS, 378, 198
Graham A. W., Onken C. A., Athanassoula E., Combes F., 2011, MNRAS, 412, 2211 (G011)
Greene J. E., Ho L. C., Barth A. J., 2008, ApJ, 688, 159
Greene J. E., Peng C. Y., Ludwig R. R., 2010, ApJ, 709, 937
Gültekin K. et al., 2009a, ApJ, 695, 1577
Gültekin K. et al., 2009b, ApJ, 698, 198
Hambly N. C. et al., 2008, MNRAS, 384, 637
Häring N., Rix H. W., 2004, ApJ, 604, L89
Henkel C., Braatz J. A., Greenhill L. J., Wilson A. S., 2002, A&A, 394, L23
Herrnstein J. R., Moran J. M., Greenhill L. J., Diamond P. J., Miyoshi M., Nakai N., Inoue M., 1997, ApJ, 475, L17
Herrnstein J. R. et al., 1999, Nat, 400, 539
Hewett P. C., Warren S. J., Leggett S. K., Hodgkin S. T., 2006, MNRAS, 367, 454
Hu J., 2009, preprint (arXiv:0908.2028) (H09)
Huchra J., Davis M., Latham D., Tonry J., 1983, ApJS, 52, 89
Ivanov V. D., Alonso-Herrero A., 2003, Ap&SS, 284, 565
Jahnke K. et al., 2009, ApJ, 706, L215
Jarrett T. H., Chester T., Cutri R., Schneider S., Skrutskie M., Huchra J. P., 2000, AJ, 119, 2498
Jerjen H., Binggeli B., Barazza F. D., 2004, AJ, 127, 771
Jones D. L., Wehrle A. E., Meier D. L., Piner B. G., 2000, ApJ, 534, 165
Kent S. M., 1987, AJ, 94, 306
Kent S. M., 1990, MNRAS, 247, 702
Kent S. M., Dame T. M., Fazio G., 1991, ApJ, 378, 131
Kim M., Ho L. C., Peng C. Y., Barth A. J., Im M., Martini P., Nelson C. H., 2008, ApJ, 687, 767
Kormendy J., Gebhardt K., 2001, in Wheeler C. J., Martel H., eds, AIP Conf. Proc. Vol. 586, Relativistic Astrophysics. Am. Inst. Phys., Melville, p. 363
Kormendy J., Richstone D., 1995, ARA&A, 33, 581
Kormendy J. et al., 1997, ApJ, 482, L139
Kormendy J., Kennicutt R. C., Jr, 2004, ARA&A, 42, 603
Kormendy J., Fisher D. B., Cornell M. E., Bender R., 2009, ApJS, 182, 216 (KF09)
Krajnović D., Cappellari M., de Zeeuw P. T., Copin Y., 2006, MNRAS, 366, 787
Lauer T. R. et al., 1995, AJ, 110, 2622
Lauer T. R. et al., 1996, ApJ, 471, L79
Lawrence A., Warren S. J., Almaini O., Edge A. C., Hambly N. C., Jameson R. F., Lucas P., Casali M., 2007, MNRAS, 379, 1599
Liske J., Lemon D. J., Driver S. P., Cross N. J. G., Couch W. J., 2003, MNRAS, 344, 307
Lodato G., Bertin G., 2003, A&A, 398, 517
Macchetto F., Marconi A., Axon D. J., Capetti A., Sparks W., Crane P., 1997, ApJ, 489, 579

Maciejewski W., Binney J., 2001, MNRAS, 323, 831
McLeod K. K., Bechtold J., 2009, ApJ, 704, 415
McLure R. J., Dunlop J. S., 2002, MNRAS, 331, 795
Magorrian J. et al., 1998, AJ, 115, 2285
Mahdavi A., Trentham N., Tully R. B., 2005, AJ, 130, 1502
Marconi A., Hunt L. K., 2003, AJ, 589, L21
Merritt D., Ferrarese L., Joseph C. L., 2001, Sci, 293, 1116
Moellenhoff C., Hummel E., Bender R., 1992, A&A, 255, 35
Möllenhoff C., Heidt J., 2001, A&A, 368, 16
Nieto J. L., McClure R., Fletcher J. M., Arnaud J., Bacon R., Bender R., Comte G., Poulain P., 1990, A&A, 235, L17
Novak G. S., Faber S. M., Dekel A., 2006, ApJ, 637, 96
Nowak N., Saglia R. P., Thomas J., Bender R., Pannella M., Gebhardt K., Davies R. I., 2007, MNRAS, 379, 909
Pastorini G. et al., 2007, A&A, 469, 405
Peng C. Y., Impey C. D., Ho L. C., Barton E. J., Rix H., 2006, ApJ, 640, 114
Peng C. Y., Ho L. C., Impey C. D., Rix H.-W., 2010, AJ, 139, 2097
Peterson B. M. et al., 2004, ApJ, 613, 682
Quillen A. C., Bower G. A., Stritzinger M., 2000, ApJS, 128, 85
Rest A., van den Bosch F. C., Jaffe W., Tran H., Tsvetanov Z., Ford H. C., Davies J., Schafer J., 2001, AJ, 121, 2431
Rix H., Carollo C. M., Freeman K., 1999, ApJ, 513, L25
Sarzi M., Rix H., Shields J. C., Rudnick G., Ho L. C., McIntosh D. H., Filippenko A. V., Sargent W. L. W., 2001, ApJ, 550, 65
Schlegel D. J., Finkbeiner D. P., Davis M., 1998, ApJ, 500, 525
Scoville N. Z., Matthews K., Carico D. P., Sanders D. B., 1988, ApJ, 327, L61
Seigar M. S., Graham A. W., Jerjen H., 2007, MNRAS, 378, 1575
Sérsic J. L., 1968, Atlas de Galaxias Australes. Obser. Astron., Córdoba
Shen J., Gebhardt K., 2010, ApJ, 711, 484
Shields G. A., Menezes K. L., Massart C. A., Vanden Bout P., 2006, ApJ, 641, 683
Siopis C. et al., 2009, ApJ, 693, 946
Soria R., Graham A. W., Fabbiano G., Baldi A., Elvis M., Jerjen H., Pellegrini S., Siemiginowska A., 2006, ApJ, 640, 143
Tonry J. L., Dressler A., Blakeslee J. P., Ajhar E. A., Fletcher A. B., Luppino G. A., Metzger M. R., Moore C. B., 2001, ApJ, 546, 681
Tremaine S. et al., 2002, ApJ, 574, 740
Treu T., Woo J., Malkan M. A., Blandford R. D., 2007, ApJ, 667, 117
Trujillo I., Erwin P., Asensio Ramos A., Graham A. W., 2004, AJ, 127, 1917
Valluri M., Merritt D., Emsellem E., 2004, ApJ, 602, 66
van den Bosch F. C., Ferrarese L., Jaffe W., Ford H. C., O'Connell R. W., 1994, AJ, 108, 1579
van der Marel R. P., van den Bosch F. C., 1998, AJ, 116, 2220
Verolme E. K. et al., 2002, MNRAS, 335, 517
Vika M., Driver S. P., Graham A. W., Liske J., 2009, MNRAS, 400, 1451
Walsh J. L., Barth A. J., Ho L. C., Filippenko A. V., Rix H., Shields J. C., Sarzi M., Sargent W. L. W., 2008, AJ, 136, 1677
Walter F., Carilli C., Bertoldi F., Menten K., Cox P., Lo K. Y., Fan X., Strauss M. A., 2004, ApJ, 615, L17
Weinzirl T., Jogee S., Khochfar S., Burkert A., Kormendy J., 2009, ApJ, 696, 411
Woo J.-H., Treu T., Malkan M. A., Blandford R. D., 2006, ApJ, 645, 900
Zezas A., Birkinshaw M., Worrall D. M., Peters A., Fabbiano G., 2005, ApJ, 627, 711
Zhao J.-H., Sumi D. M., Burns J. O., Duric N., 1993, ApJ, 416, 51

APPENDIX A: GALFIT3 σ MAP

In this paper, we profiled a sample of 29 galaxies by allowing GALFIT3 to create the σ (weight) maps internally. In this section, we want to repeat the fit for the full sample by providing an external σ map for each galaxy. The construction of the external maps is based on the same formulae that GALFIT3 uses internally:

$$\sigma^{[\mathrm{ADU}]}(x, y) = \frac{\sqrt{\sigma_d^{[\mathrm{e}^-]}(x, y)^2 + \sigma_{\mathrm{sky}}^{[\mathrm{e}^-]}(x, y)^2}}{\mathrm{gain}}, \quad \text{(A1)}$$

$$= \sqrt{\frac{f_d^{[\mathrm{ADU}]}(x, y) - \mathrm{sky}^{[\mathrm{ADU}]}}{\mathrm{gain}} + \sigma_{\mathrm{sky}}^{[\mathrm{ADU}]}(x, y)^2}, \quad \text{(A2)}$$

where

$$\sigma_d^{[\mathrm{e}^-]}(x, y) = \sqrt{(f_d^{[\mathrm{ADU}]}(x, y) - \mathrm{sky}^{[\mathrm{ADU}]})}, \quad \text{(A3)}$$

where $f_d(x, y)$ is the image flux at pixel (x, y) in ADU units, sky is the sky value listed in Table 2, gain is equal to 4.5 e^- ADU^{-1} and $\sigma_{\mathrm{sky}}(x, y)$ is the full resolution noise map of the sky background created by SExtractor. The σ map shows the flux uncertainty at each pixel, and the construction is based on Poisson statistics. The created σ map is compatible with GALFIT3 and can replace the internal σ map.

After the σ map has been created, we re-run GALFIT3 using as input/starting values the best-fitting values found in Table 3, but instead of permitting an internal weight map estimation, we provide the external weight map. Fig. A1 shows that there is no significant change in using a GALFIT3 internal σ map or a SExtractor external σ map.

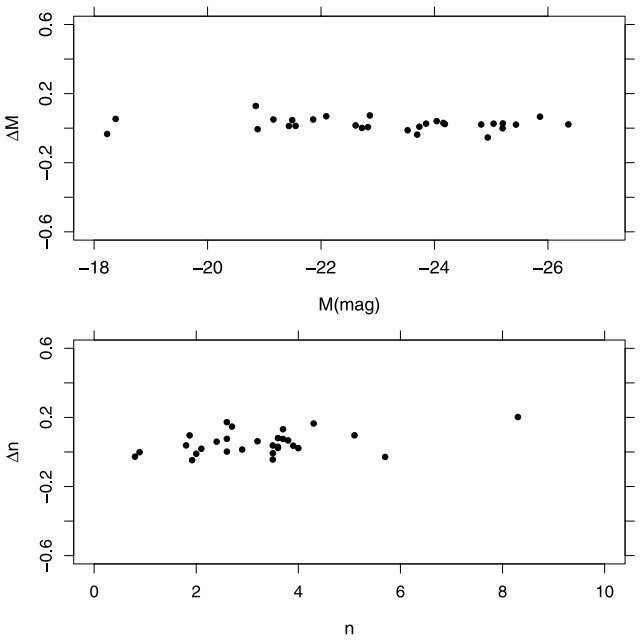

Figure A1. Top panel: a plot of the GALFIT3 magnitude differences found using either an internal σ map or an external σ map against the range of internal magnitudes. Bottom panel: the same for the Sérsic index.

This paper has been typeset from a TEX/LATEX file prepared by the author.